Strong Field Dynamics and Control of Molecular Dissociation

A Dissertation Presented

by

Sarah Roxanna Nichols

to

The Graduate School

in Partial Fulfillment of the Requirements

for the Degree of

Doctor of Philosophy

in

Physics

Stony Brook University

December 2008

Stony Brook University

The Graduate School

Sarah Roxanna Nichols

We, the dissertation committee for the above candidate for the Doctor of Philosophy degree, hereby recommend acceptance of this dissertation.

Thomas Weinacht – Dissertation Advisor
Associate Professor, Department of Physics and Astronomy

Harold Metcalf – Chairperson of Defense
Distinguished Teaching Professor, Department of Physics and Astronomy

Jacobus Verbaarschot
Professor, Department of Physics and Astronomy

Tamás Rozgonyi
Researcher, Institute of Structural Chemistry
Chemical Research Centre of the Hungarian Academy of Sciences
Budapest 1525 Hungary

This dissertation is accepted by the Graduate School.

Lawrence Martin
Dean of the Graduate School

Abstract of the Dissertation

Strong Field Dynamics and Control of Molecular Dissociation

by

Sarah Roxanna Nichols

Doctor of Philosophy

in

Physics

Stony Brook University

2008

Ultrafast lasers allow for the investigation of chemical reactions on their own natural time scale, much as a strobe light allows the visualization of rapid motion on a camera. The strong electric fields of amplified ultrafast lasers can be used not only to observe a chemical reaction, but also to control it. In this thesis, we present observations of molecular dissociation dynamics and evidence of control in several small molecules. We begin with a discussion of alignment dynamics, whereby field-free alignment is initiated in a sample of gas-phase molecules prior to ionization and dissociation. This enhances the ionization effectiveness of subsequent laser pulses, particularly for diatomic molecules such as N_2 and O_2, as the molecular axis can be aligned with the laser polarization.

We continue with a discussion of dissociation dynamics in a family of small molecules, focusing on halogen-substituted methanes (halomethanes). Halomethanes are small enough to allow for detailed electronic structure calculations, while being large enough to be chemically relevant and offer opportunities for selective dissociation. We find that dissociation in halomethanes is controlled by the development of transient ionic resonances, which can be accessed by a weak probe pulse following the ionizing pump pulse. These dynamic resonances create strong oscillatory behavior in the experimental ion yields, which can be modeled by wave packet calculations on *ab initio* potential energy surfaces. We find excellent quantitative agreement between the calculations and the experimental measurements, yielding a detailed understanding of the dissociation dynamics of some members of the halomethane family, including CH_2BrI. Ongoing work focuses on better understanding differences between members of the molecular family. This understanding may have implications for control and dissociation dynamics in larger, more complicated molecules.

Contents

List of Figures

List of Tables

Acknowledgements

Thanks to my advisor, Tom Weinacht, for all of his support and help over the years, and for teaching me all sorts of things, ranging from how to clean a grating to how to write a good conference abstract. Thanks to Tamás Rozgonyi for extensive aid in exploring the implications of molecular structure calculations on our experimental results. All calculated potentials shown in this work are his, unless noted otherwise. Thanks to Harold Metcalf for his support on both this thesis and physics in general - he helps keep AMO at Stony Brook fun and productive. Thanks to Jac Verbaarschot for an excellent instruction in the fundamentals of quantum mechanics. Thanks to Brett Pearson for his excellent advice on both lab and career topics. To the other members of the lab, past and present: Jay Brown, Dave Cardoza, Steve Clow, Marty Cohen, Dan Flickinger, Dominik Geißler, Brendan Keller, Florian Langhojer, Marija Kotur, Evan Raba, Carlos Trallero-Herrero, and Coco Tseng: thanks for providing a sounding board for ideas and a spare pair of hands in the lab.

Thanks are also due to those outside the group. The Metcalf and Schneble groups were always willing to lend a sympathetic ear or a crucial piece of equipment, as needed, and I appreciate it. Thanks to the staff of the machine shop, particularly Walt Schmeling and Jeff Slechta, without whom my molecular beam chamber would be little more than a handful of sketches. And thanks to all the main office staff, who made everything administrative as easy as possible and always greeted me with a smile.

While at Stony Brook I was supported by an Optics Fellowship and a Graduate Council Fellowship, and I am grateful for the opportunities these fellowships gave me. The research described herein was supported by the National Science Foundation, the Research Foundation, and the American Chemical Society.

Several researchers engaged in helpful discussions which helped to clarify our thoughts, particularly on the material in Chapter 3. I am grateful to Mark Baertschy, Ryan Coffee, George Gibson, and Markus Guehr for their input.

Numerous friends inside and outside the department provided good food and good company, as well as sympathy for the ups and downs of graduate school. Although I cannot list everyone, my especial thanks to Jen Barone, Sarah Campbell, Justin Georgi, Melissa Georgi, Joe Groenke, Ken Herner, Chris Holmes, Kate Oheim, Jason Reeves, Katie Saxon, Gina Sorrentino, Jessica Stanton, and Anne Su. You made this journey a lot more fun.

Finally, thanks to my family for their support over the years. Mom, Dad, and Sami, you were always encouraging, and always willing to listen, even when I baffled you with complex quantum mechanical descriptions. Thank you for your patience and your love. Last, but certainly not least, thanks to my husband Andy Farke for your incredible love and unwavering support every step of the way. You kept me laughing at work and at play.

Chapter 1

Introduction

Chemical reactions (*e. g.*, bond breaking and formation, molecular vibrations, etc.) take place on timescales of femtoseconds to picoseconds, which is too fast to be observed with methods that rely on electronic or physical switches. Moreover, on long time scales, the excitation of one mode is transferred to smaller excitations of many modes, complicating observations. However, with the advent of ultrafast lasers, experimental measurements have been able to track the influence of coherent wave packet motion during simple chemical reactions such as bond breaking before energy is statistically redistributed in the molecule [1]. We seek to understand and control chemical reactions in small molecules ($\lesssim$ 10 atoms) by applying a sequence of shaped laser pulses. We then use the pulse shapes and resulting molecular fragments to infer the dynamics of the quantum wave packets involved in the reactions.

Interest in laser selective chemistry [2, 3] and molecular imaging [4–8] has driven many advances in our understanding of the interaction of molecules with intense, ultrafast laser fields. Developments in ultrafast laser technology have permitted the generation of shorter pulses and greater control over them, benefitting the study of strong-field molecular photofragmentation. The field is especially rich, as it involves both resonant and off-resonant electronic transitions, vibrational wave packets, and multiple interfering pathways to fragment dissociation. Different models have been proposed to explain the observed photoionization and fragmentation patterns in ion time-of-flight mass spectra for various molecular families (for example, see [9–16]).

In a typical pump-probe gas phase femtochemistry experiment, an ultrafast pump pulse excites a coherent superposition of vibrational eigenstates on a potential energy surface, leading to time-dependent evolution of the nuclear coordinate expectation values. For femtosecond laser pulses with peak intensities where the Keldysh parameter [17], $\gamma = \omega_{laser}/\omega_{tunneling}$, is less than one, tunnel ionization takes place rapidly, leading to substantial ionization on the

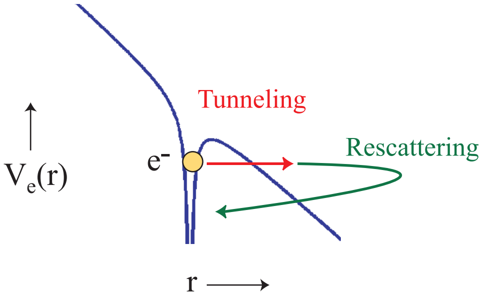

Figure 1.1: A schematic diagram of electron tunneling, followed by rescattering in a subsequent oscillation of the field.

rising edge of the pulse [11]. This tunnel ionization can be pictured by superposing the potentials of a strongly bound electron (deep well) and a strong electric field (steep linear slope). When the field is strong enough (the slope is very steep), the electron can tunnel out through the low barrier in less than the half-cycle oscillation time for the field. Often the electron will continue to oscillate in the field, and may recollide with the ion from which it came. This rescattering process may result in the promotion of the ion to a higher energy state, or in further ionization events. Figure 1.1 shows a simple schematic of the tunnel ionization and rescattering events.

Generally, there are multiple ionic states available, because there are multiple electron orbitals. In contrast with atomic systems, the energies associated with ionizing from many of these orbitals may be quite similar. Thus, ionic resonances in the near infrared are common in small polyatomic molecules with many electrons [12] as a result of the low cost in energy associated with moving the electron hole left by ionization around the molecule. Furthermore, since the equilibrium geometry of the ion is generally different than that of the neutral molecule, ionization can produce large amplitude vibrational motion in the ion that leads to inherently dynamic resonances [18]. Thus one expects that ionic resonances in the infrared are common, dynamic, and important for understanding the dissociation of small polyatomic molecules in intense ultrafast laser fields [16].

Therefore, a weak infrared probe pulse that comes in after the ion has been created may be able to dynamically access several ionic states. Varying the delay of a subsequent probe pulse can control the final bond breaking yield by modifying the excitation probability to a final potential energy surface where the wave packet moves toward dissociation. The timing of the probe pulse determines whether the wave packet is in the Franck-Condon (FC) region for transfer to the final state, and thus these experiments rely on the evolution of the probability density on the intermediate state surface. The dissociation probability is modulated by the coherent vibrational motion of the wave packet, but the reaction dynamics often are driven by the wave function probability density [19, 20].

Recent studies have examined the role that ionic resonances play in the fragmentation process [15, 21–23]. Specifically, it has been suggested that single-photon resonances in the molecular ion provide efficient pathways to multiple fragmentation channels [12, 15, 21]. Other studies have found molecular systems that appear to show little or no fragmentation despite having single-photon absorptions from the ionic ground state [22]. Although the static absorption spectrum of the ion may be useful in cases where the neutral and ionic equilibrium geometries are similar, when they are substantially different, wave packet motion in the ionic state can lead to dynamic resonances that must be taken into account in order to understand the fragmentation pattern. Alignment effects may also play a role, as the alignment of molecular orbitals relative to the laser polarization axis can affect ionization and dissociation.

The tools of laser femtochemistry can be applied to many systems, but in our lab we have chosen to focus on small molecules (5-10 atoms or fewer). These small molecules are in an ideal size range, where there is more than a single degree of spatial freedom (as in a diatomic molecule), but the molecules are still small enough to offer a reasonable possibility of *ab initio* structure calculations. Also, although there may be more than one reaction coordinate (important degree of freedom), there are not so many that the dynamics of dissociation are too difficult to understand. This thesis presents the results of several femtochemistry experiments performed in our lab and compares some of the results with the calculational results of our collaborators. The reader may also wish to refer to previous results [24] and to current work [25, 26] from our group.

We start with a description of our experimental setup in Chapter 2, including both the laser system used in the lab and the molecular beam chamber that I designed and built in order to examine molecular rotational dynamics. Chapter 3 continues with a discussion of the alignment experiments, both in the diatomic molecules N_2 and O_2 and in the larger molecule CH_3COCF_3. Chapter 4 contains an extended discussion of the halomethane experiments that have formed the bulk of this thesis. We finish with some concluding remarks in Chapter 5.

Chapter 2

Experimental Apparatus

2.1 Laser

Our measurements begin with pulses from an amplified titanium:sapphire laser system (30 fs, 1 mJ, 1 kHz repetition rate) that are subsequently split in a Mach-Zehnder interferometer (see Figure 2.1). One arm of the interferometer contains a pulse shaper (Figure 2.2, described further below) with a computer-controlled acousto-optic modulator (AOM) as the shaping element [27]. The AOM can control the energy (intensity), duration, and chirp of either the pump or probe pulse. The two pulses are focused and intersect in an effusive molecular beam inside a vacuum chamber equipped with a time-of-flight mass spectrometer (TOFMS) that resolves the different fragment ions. Peak pump-pulse intensities are approximately 1.7×10^{14} W/cm^2, with typical pulse durations of 30–40 fs. The shortest possible pulse, given our bandwidth, is described as a transform-limited (TL) pulse. In our system, transform-limited pulses are 30–35 fs, depending on the path of the pulse. For a more detailed description of the experimental apparatus see [28].

The pulse shaper uses the method developed by Weiner [29]. The pulses enter and are bounced off of a grating, which spreads the frequencies in the horizontal plane, as seen in Fig. 2.2. The dispersing beam is then collimated by a curved mirror. In the Fourier plane of the curved mirror, we place an AOM, which acts as a programmable mask to control the phase and amplitude of each input frequency. Using a radio-frequency generator, we create an acoustic wave in the AOM. The resulting density modulation in the crystal acts as a transmission diffraction grating, where the position-dependent amplitude of the acoustic wave at each point along the crystal causes an amplitude variation for the corresponding optical frequency, while the phase of the acoustic wave controls the phase of the corresponding optical frequency. Thus, by controlling

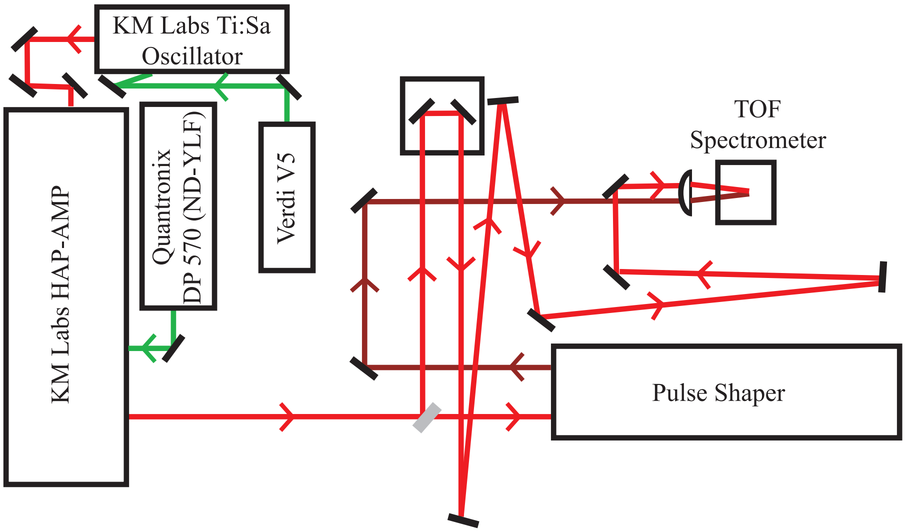

Figure 2.1: A diagram of our laser apparatus, showing the two arms of the Mach-Zehnder interferometer.

the acoustic wave at each spatial position in the crystal, we can control the phase and amplitude of each component frequency in our laser pulse. The second half of the pulse shaper inverts the spatial dispersion introduced in the first half, using the first-order diffracted beam from the AOM, to create a collimated, shaped pulse.

We can also use the pulse shaper to search for an optimal pulse for a particular task. If we feed the experimental results from a given pulse shape back to the computer, the computer can iteratively search for an optimal pulse using a learning control algorithm [30, 31]. Our search algorithm is called a genetic algorithm (GA), for its resemblance to the natural selection that operates in biological systems [32]. The details of our algorithm are described in [28, 33].

Pulses can be characterized using either a second harmonic generation frequency-resolved optical gating (SHG-FROG) apparatus [34, 35] or with a GRating-Eliminated No-nonsense Observation of Ultrafast Incident Laser Light E-fields (GRENOUILLE) device [36, 37], both of which were built in the lab by other students. A typical SHG-FROG output for a TL pulse from the shaped arm of the interferometer is shown in Figure 2.3.

Experimental results, whether from a molecular time-of-flight signal or a photodiode, are recorded using a 500 MHz, 8-bit computer based oscilloscope (GAGE Compuscope 8500). Most signals are preamplified before entering the GAGE oscilloscope using a 350 MHz amplifier (Stanford Research Systems

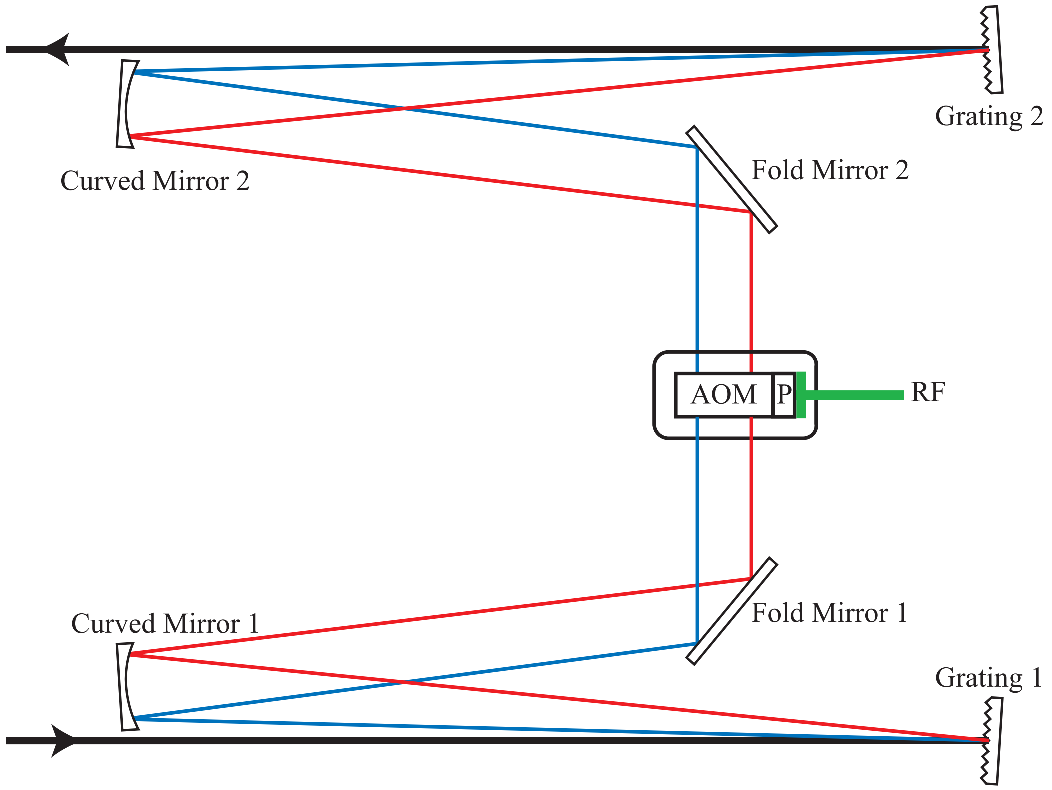

Figure 2.2: The pulse shaper, which uses the typical 4f configuration [27].

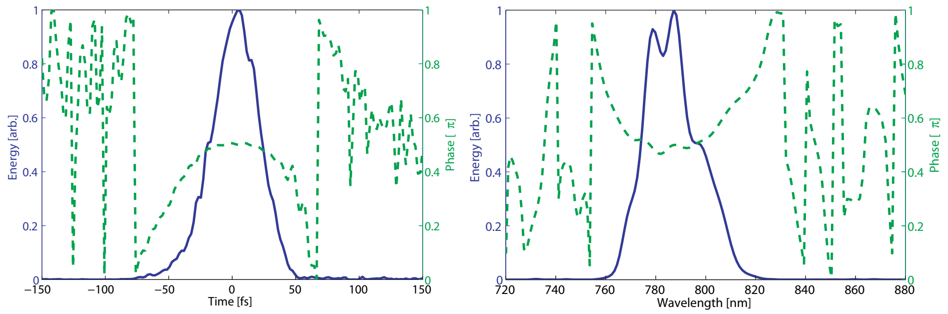

Figure 2.3: A typical SHG-FROG output for the shaped arm of the pulse shaper, when no shaping is applied (TL pulse). The raw SHG-FROG trace is used to reconstruct the intensity and phase of the pulse as a function of time (left) and wavelength (right).

SIM 914). The computer-based oscilloscope is programmed and the results recorded using Labview [38].

2.2 Molecular Beam Chamber

Previous experiments in the lab used an effusive source for gas phase molecules [33, 35]. Although effusive sources have the benefit of being simple to build and operate, they are limited to producing room temperature molecules with the full distribution of rotational and vibrational quantum states. For certain experiments, it is useful to have cooled molecules, with a limited number of low-lying rotational states. We also wanted to improve the resolution of previous TOFMS setups in the lab. Thus, we designed and built the chamber shown in Figure 2.4, relying heavily on [39].

The chamber uses a turbo pump (Varian Turbo-V 301 Navigator) and a diffusion pump (a refurbished Varian VHS-6) to provide the differential pumping required for a good molecular beam. All high-vacuum regions were constructed of stainless steel in the department machine shop, with ConFlat (copper gasket) seals. The nozzle and skimmer for the molecular beam were purchased from Beam Dynamics, Inc., and mounted with a gold o-ring and a Viton gasket, respectively. The nozzle-skimmer distance can be adjusted using the bellows apparatus on the right hand side of Fig. 2.4. Some portions of the lower vacuum (*i. e.*, roughing lines) are aluminum construction, with standard wire-reinforced PVC hose used for the roughing lines themselves. The whole chamber is supported on a Unistrut frame, which is isolated from the lab optical tables. Laser beams are picked off just before the focusing lens in Fig. 2.1, and the parallel pump and probe beams are directed into the chamber through free space using a combination of periscopes and breadboards. The laser beams enter through a thin sapphire window.

The time-of-flight (TOF) section of the chamber is where the molecules are detected in either of two ways. The simpler method (but not time-resolved) is to use the Extorr residual gas analyzer (RGA), which measures the partial pressure by molecular weight of all gaseous contents of the chamber (up to a mass of 200 amu). This is extremely useful for contaminant detection, either of contaminants intrinsic to the chamber (H_2O, N_2, O_2) or of contaminants occurring in our liquid samples (for instance, many halomethane compounds will break down with time and/or exposure to UV radiation, leading to a substantial contaminating fraction of halogen diatomics). For most experimental detection we use the TOF mass spectrometer (TOFMS), a portion of which is shown schematically in Figure 2.5. We use single-stage extraction, with a charge of 750 V on the bottom plate and a plate separation of 0.9 cm. The

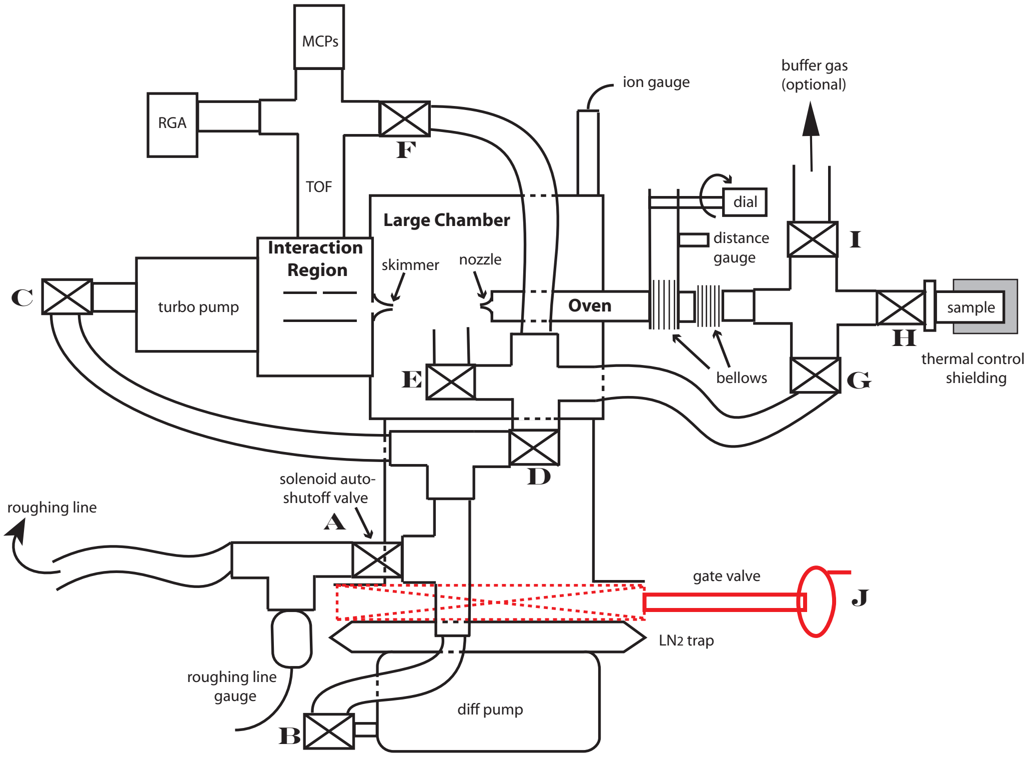

Figure 2.4: The molecular beam chamber (not to scale). Valves are labeled alphabetically for ease of procedural reference.

molecules enter from the right hand side and are ionized by the laser beam, which enters perpendicular to the plane of Figs. 2.4 and 2.5. The ions then move upward in the field of the plates and go through the small hole (500 μm) in the top plate. The ions continue upward through a relatively field-free TOF region and hit the microchannel plates (MCPs). The voltage gap across the MCPs creates a factor of 10^6 enhancement in the ion signal, much as a photodiode enhances an optical signal by creating an electron cascade. The new chamber is substantially cleaner than the previous one, as seen in Figure 2.6, which compares the TOF traces produced by the old chamber (panel a) and the new chamber (panel b and inset) with a sample of 1,1,1-trifluoroacetone (CH_3COCF_3). The resolution is greatly increased in the new chamber: the usual figure of merit is $\frac{m}{\Delta m}$, where m is the mass/amu of a particular peak and Δm is the full width at half maximum (FWHM) of that peak. The old chamber had a resolution of 50, while the new chamber has a resolution of 200, or 4 times better. The new chamber also has a greatly reduced contaminant signal, as seen by comparing the inset of Fig. 2.6b to Fig. 2.6a. The N_2^+ and O_2^+ peaks are negligible, and the H_2O^+ signal is no longer visible[1]. Other peaks such as H^+, which may result from roughing pump oil that has backstreamed into the chamber, have also been eliminated.

Several factors improve the cleanliness of the molecular beam chamber. The all-stainless construction of the main body of the chamber means that the chamber can be baked at higher temperatures (typically 160 °C) than the effusive chambers (typically 70 °C), which are limited by the Viton o-ring gaskets of their Quick Flange (KF) seals. The higher flow rates (and thus lower resulting vacuum pressures) of the diffusion and turbo pumps also mean that fewer molecules adhere to the sides of the chamber, leading to lower desorption rates later. With no sample, pressures in the main chamber are in the low 10^{-7} torr when the turbo pump is pumping on all parts of the chamber, or in the mid 10^{-9} torr when the turbo and diffusion pumps are both operating in differential pumping mode.

Samples are admitted to the chamber through valve H of Fig. 2.4. The sample chamber is designed for admitting gaseous molecules. For instance, N_2 and O_2 can be admitted directly into the chamber from a tank through a flow-limiting leak valve. Alternately, liquid (halomethanes and many other small organic molecules) and even solid molecules (I_2) may be used to provide sample, as long as they can be held at an appropriate temperature to provide a moderate vapor pressure. Although not used in the experiments described

---

[1] Despite being "contaminants", all three ions provide useful points of comparison. Their high ionization potentials ($\sim$ 12–15 eV [40]) relative to our photon energy of 1.58 eV result in a sharp peak from the nonlinear pulse overlap at time zero when the Mach-Zender delay stage is scanned, which we use to pinpoint our absolute time delay.

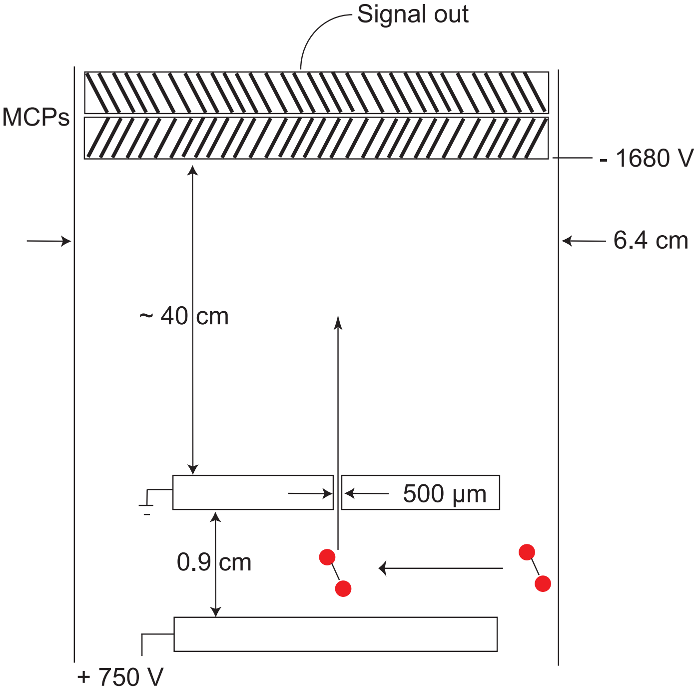

Figure 2.5: A TOF schematic (not to scale). Some functionally important dimensions are marked.

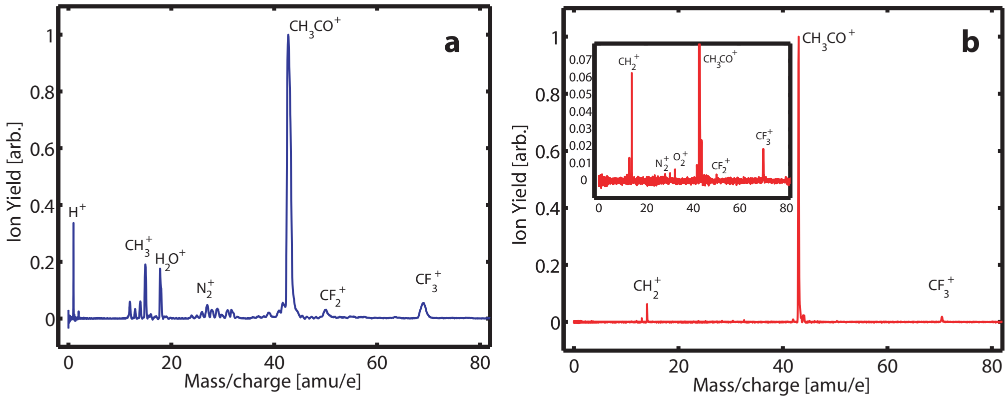

Figure 2.6: TOFMS for CH_3COCF_3 in a) the old chamber and in b) the new chamber. Note the increased resolution (narrower peaks) and the greatly reduced contamination signal (inset).

in this thesis, we also have the capability to simultaneously admit a buffer gas such as argon (Ar) through valve I. Inert buffer gases are frequently used in molecular beam systems to provide further cooling, as the molecules of interest can transfer energy to the buffer gas through collisions [39]. Typical running pressures are around 1 torr in the sample chamber, 10^{-4} torr in the main chamber, and 5×10^{-7} torr in the sample chamber.

The combination of laser characteristics such as a 30 fs timescale, broad bandwidth in the same spectral region as many molecular resonances, and pulse shaping ability with a clean molecular beam and high resolution time-of-flight detection system gives us a great deal of flexibility in performing molecular chemistry experiments. The alignment experiments of Chapter 3 will especially highlight the molecular beam chamber. The description of the halomethane dissociation experiments in Chapter 4 will demonstrate the broad range of available laser pulses.

Chapter 3

Molecular Alignment

Most molecules are asymmetric along one or more dimensions, and have non-uniform polarizabilities. This anisotropic polarizability means that molecules can be aligned, either by a static or a transient field. For many molecules, the control pulses we apply depend on the dipole moment of a particular electronic transition, and thus on the alignment of the molecule relative to the laser polarization. In many cases it would be helpful to have a sample of aligned molecules so as to improve our degree of control over a given chemical reaction. As discussed by Seideman [41–43], for rotationally cold samples, a femtosecond pulse can be used to create a rotational wave packet. As the rotational frequencies are proportional to $j(j+1)$, waiting the appropriate time interval after the laser pulse means that all rotational states have come into phase again. The sample is therefore aligned while in a field-free region. This is far preferable to both static alignment with a permanent field and adiabatic alignment with a long (picosecond or longer) laser pulse. Permanent fields large enough to align molecules are extremely difficult to create experimentally over macroscopic distances, and for adiabatic alignment one has to consider the interaction of the molecule with two fields: the long pulse alignment field and the short pulse laser field that induces the dynamics of interest. Pulses of intensity $\sim 10^{12}$ W/cm^2 are sufficient to align most molecules while avoiding ionization [43].

Figure 3.1 shows a simple schematic of the relevant components. A rigid rotor molecule is exposed to a pulsed electric field $\varepsilon(t)$ with linear vertical polarization. The molecular polarizability tensor α has a primary component along the molecular axis ($\alpha_{\|}$) and a secondary component perpendicular to it ($\alpha_{\perp}$). The electric pulse "kicks" the molecule, pushing it into alignment with

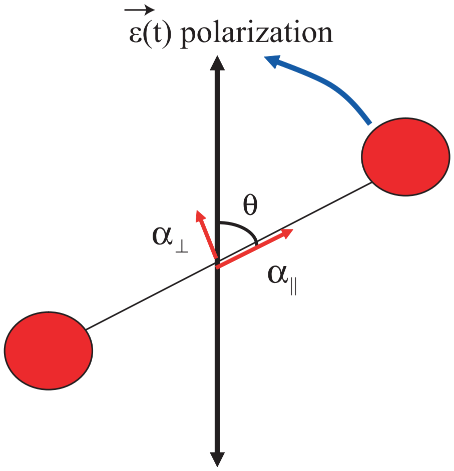

Figure 3.1: A diagram of alignment in a simple rigid rotor molecule. $\alpha_\parallel$ and $\alpha_\perp$ are components of the polarizability tensor, and θ is the angle between $\alpha_\parallel$ (usually along the major axis of the molecule) and the laser pulse polarization.

the polarization. The Hamiltonian in this simple case is given by

$$H(t) = H_0 - \frac{1}{2}\varepsilon(t)^2 \left(\Delta\alpha \cos(\theta)^2 + \alpha_\perp\right),$$

where $\Delta\alpha = \alpha_\parallel - \alpha_\perp$. The molecules will initially be aligned, with all their $\alpha_\parallel$ axes parallel. However, the molecules will not be orientationally selected; that is, given a diatomic molecule A-B and vertical polarization, alignment means either A or B may be on top, as long as the A-B axis is vertical. Orientation would imply that only A's (or only B's) were on top. Orientation does not take place because in general a short pulse has several field oscillations under the pulse envelope, so there is no preferred direction along the polarization axis.

After the molecules are kicked into alignment, their angular momentum has not been removed, so the rotation continues. This initially causes an anti-alignment, where the A-B axes are all in the plane perpendicular to the laser polarization (linear polarizations can only align along one dimension, so there is no preferred anti-alignment direction). Because the molecules are not all in the same rotational state, the alignment subsequently dephases. As noted above, however, with only a few low rotational eigenstates present, the molecules remain coherent and waiting the appropriate amount of time will bring them into alignment again. The degree of alignment of a collection of molecules is generally measured as

$$\langle\cos^2\theta(t)\rangle = \int \psi^*(t)\cos^2\theta\,\psi(t)\,\mathrm{d}\theta.$$

An unaligned (uniform distribution) two-dimensional sample has $\langle\cos^2\theta\rangle = 0.5$, and a three-dimensional sample has $\langle\cos^2\theta\rangle = 0.33$.

Our alignment apparatus was built with the goal of aligning large molecules in which we had previously demonstrated short-pulse control. One such molecule is 1,1,1-trifluoroacetone, CH_3COCF_3. This highly asymmetric molecule was the subject of previous control experiments in the group [28, 44, 45], which showed that control of CF_3^+ production depended on enhanced ionization and was sensitive to the polarization of the laser relative to the TOF detector axis. We hoped to show that alignment would enhance the level of control. In order to test the chamber and confirm our alignment capability, we first performed experiments on N_2, a diatomic whose alignment and ionization have been well-studied [6, 46–50].

3.1 Nitrogen Alignment

When we put N_2 molecules in our chamber and apply a laser pulse, the laser ionizes the molecules as well as aligning them. When we scan the pump probe delay of our laser, we see the expected 8.4 ps revival structure in our ion yield. Figure 3.2 shows the ion yield for the parent double ion N_2^{2+} over one full revival period. The increased yield just before the half revival is due to the molecules being aligned with the probe pulse polarization (here parallel to the vertical aligning pump pulse polarization). The decreased yield just after the half revival is because the molecules have all rotated 90° into the plane perpendicular to the probe polarization. This revival structure agrees well with other measurements (*e. g.*, [47]).

Our intense ultrafast laser pulse ($\sim$1–5$\times10^{14}$ W/cm^2) creates several fragments, including N_2^+, N_2^{2+} and N^+ fragments. These fragments, among others, are shown in Figure 3.3. The N^+ fragments can be traced to the dissociation of both singly and doubly charged molecular ions. The kinetic energy of the N^+ fragments as measured by the TOFMS can be used to distinguish between these two possibilities. The products of the reaction $N_2^{(m+n)+} \rightarrow N^{m+} + N^{n+}$ are referred to as N^{m+}(m,n) and N^{n+}(m,n), respectively [51]. The inset of Fig. 3.3 resolves the formation of N_2^{2+}, N^+(1,0) and N^+(1,1) fragments. Only the dissociative fragments ejected along the TOFMS axis towards the detector are resolved because the dispersion of our TOFMS is not optimized for detect-

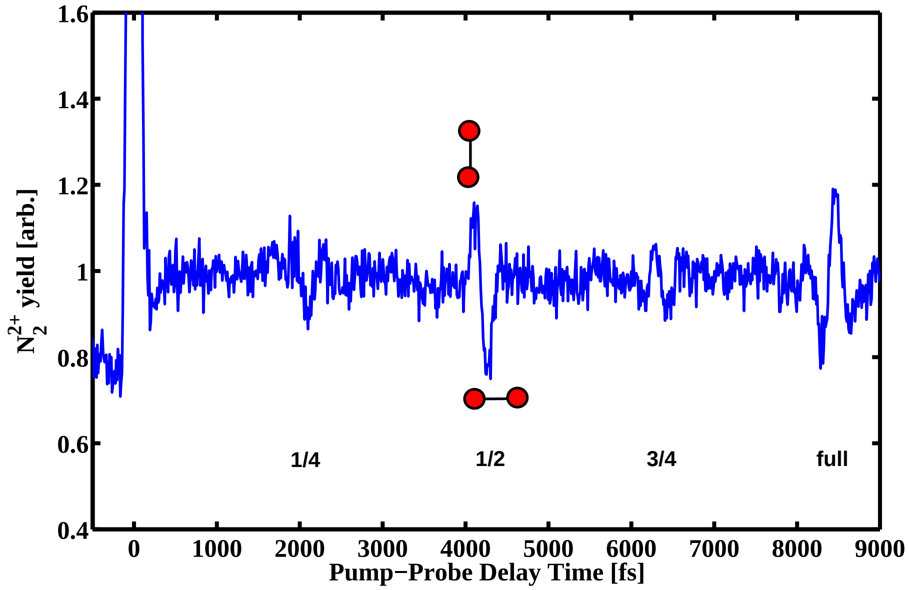

Figure 3.2: This plot shows the N_2^{2+} yield as a function of pump probe delay. The quarter, half, three-quarter, and full revival structures are clearly present. N_2 has a full revival time of 8.4 ps. The ball-and-stick models show the classical position of N_2 molecules during the alignment (vertical) and antialignment (horizontal) portions of the half-revival, assuming a vertically polarized pump pulse.

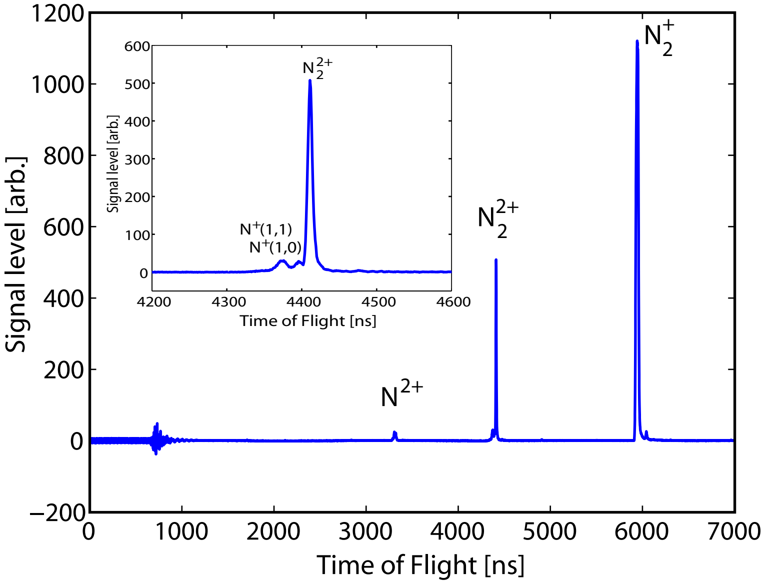

Figure 3.3: This is a typical N_2 TOFMS for two pulses at time-zero overlap. The closeup shows the separated dissociative ions.

ing energetic fragments (this is mainly due to having only a single-stage extraction field, as described in Chapter 2.2). The kinetic energies of the $N^+(1,0)$ and $N^+(1,1)$ fragments are consistent with earlier measurements [51, 52].

The double ionization that takes place during the dissociative ionization process can occur through multiple mechanisms, including barrier suppression and rescattering [53, 54]. Given our probe pulse intensity of about 1.6×10^{14} W/cm^2, we expect rescattering to be the dominant mechanism for the double ionization and formation of all three fragments [52, 55]. In order to confirm this, we measured the fragment yields as a function of polarization ellipticity. Rescattering depends strongly on the presence of a linearly polarized field — even a slight degree of ellipticity will steer the returning electron far enough from the ion to prevent rescattering. Table 3.1 shows that with a very small degree of ellipticity, the signals from the N_2^{2+}, $N^+(1,0)$, and $N^+(1,1)$ fragments all drop precipitously, but the N_2^+ signal only drops slightly. Although the projection of the major axis of the polarization ellipse and intensity of the laser both changed with the ellipticity in our measurements, independent measurements of the fragment ion yields as a function of polarization and intensity indicate that the changes noted in the table are due to the change in ellipticity and not intensity or polarization relative to the TOFMS axis.

Ellipticity ϵ	0.124	0.249
$N^+(1,1)$	72%	23%
$N^+(1,0)$	81%	21%
N_2^{2+}	74%	36%
N_2^+	96%	91%

Table 3.1: Normalized signal yield for various rotation ion fragments as a function of ellipticity. Yields are normalized to $\epsilon = 0$.

Another explanation for the ellipticity dependence is that our strong laser fields cause dynamic AC Stark shifting of intermediate electronic states [56, 57]. This means resonances can become excluded because of ellipticity dependent selection rules. We have compared our ellipticity dependence to measurements of the above threshold ionization yield in atomic argon where Stark-shifted resonances dominate the ion yield. We found that our ion signals drop more rapidly than the resonance-enhanced atomic ionization signal. The atomic ionization signal shows that at larger ellipticities (ϵ=0.378), the ion yields drop by a factor of ∼2.5 [54]. We have a larger decrease in yield, by a factor of 4–5, at smaller ellipticities. Furthermore, the effect of AC Stark shifting of resonances should be diminished in molecules as compared with atoms, because the increased number of degrees of freedom in molecules means that the selection rules are not as strict. Therefore, we believe that the drop in yield as a function of ellipticity is indeed due to rescattering. This agrees with semiclassical calculations of the rescattering electron path, which show that at the small ellipticities of our experiment, the electron misses the core (by traveling transversely on the order of a few angstroms).

Given all this, our picture thus far is that tunnel ionization initially ionizes the molecule and the continuum electron thus created can rescatter with the N_2^+ ion to produce N_2^{2+}, $N^+(1,0)$, and $N^+(1,1)$. This picture is consistent with the picture presented in reference [52] but it is not complete. Important questions remain. These include:

1. Which orbitals are initially ionized? The work of Nibarger et al. [58] suggests that we should get some mix of sigma and pi orbitals. The angular distribution of the fragments seem to indicate ionization occurs primarily from sigma electrons.

2. Does the rescattering take the molecules directly to the final product state? What states are these?

Note that similar questions about how we reach the final product state and

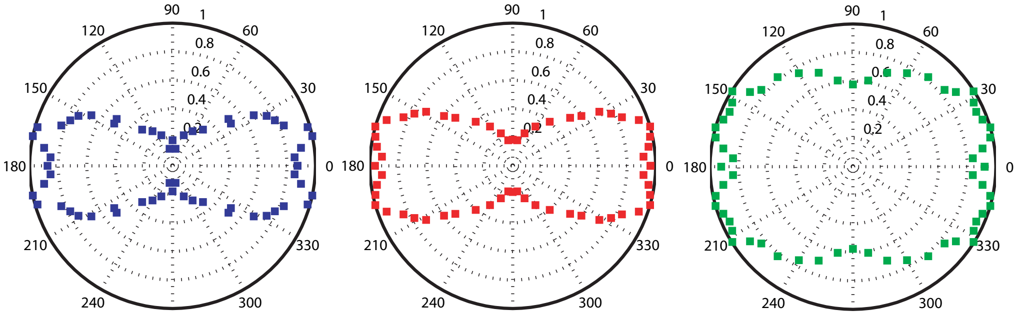

$N^+(1,1)$ ionization beam rotate signal =mean(before halfrev)*(1+fitamp)

$N^+(1,0)$ ionization beam rotate signal =mean(before half rev)*(1+fitamp)

N_2^{2+} ionization beam rotate signal =mean(before half rev)*(1+fitamp)

Figure 3.4: Polar plots of the scaled signal amplitude at a non-revival for only the ionization beam rotating. Angle is measured from the TOF axis. This is equivalent to single beam data with a slightly narrower detection function. N_2^+ (not shown) behaves similarly to N_2^{2+}.

determine its identity will come up again in Chapter 4. In order to address these questions in N_2 and complete our picture of the formation of the N_2 fragments in question, we study the angular distribution of the dissociative fragments. This can be determined directly by measuring the fragment yields as a function of the angle between the laser polarization and the TOFMS axis as a result of the narrow angular acceptance for the dissociative fragments that are produced along the molecular axis, ensuring that we essentially only collect fragments from molecules that happened to be aligned along the TOFMS axis. The relationship between the measured fragment yields as a function of angle between laser pulse polarization and TOFMS axis ($S_1(\theta)$) is given by:

$$S_{(n,m)}(\theta) = \int D(\theta')P(\theta - \theta')d\theta' \tag{3.1}$$

where $P(\theta)$ is the angular distribution of a given fragment and $D(\theta)$ is the (fragment specific) detection efficiency as a function of angle. The measured angular distributions, $S_{n,m}$ for n=1,m=0,1 are shown in Figure 3.4. Note that the angular distributions for $N^+(1,0)$, and $N^+(1,1)$ are essentially identical within the resolution of our experimental measurements. The angular distribution for the $N^+(1,1)$ channel agrees well with cold target recoil ion measurements [52]. The fact that the angular distributions for the $N^+(1,1)$ and $N^+(1,0)$ channels are the same suggests that $D(\theta)$ and $P(\theta)$ for the two channels may be similar.

For the case of the N_2^{2+} channel, there is no angular resolution in the detection of the ions[1], and we need to measure the angular distribution with the aid of a rotational wave packet. Figure 3.5 shows the N_2^{2+} yield around a half revival of a rotational wave packet created by a pump pulse roughly 4.2 ps earlier. The $N^+(1,1)$ and $N^+(1,0)$ fragments are shown for comparison. The deeper modulation in the $N^+(1,1)$ and $N^+(1,0)$ yields is a result of the angular resolution in the detection of these fragments since both laser pulses were polarized parallel to the TOFMS axis for this measurement. As the molecules come into alignment with the probe pulse and increase the probability of generating $N^+(1,1)$ and $N^+(1,0)$, the molecules are also aligned along the TOFMS axis, increasing the probability of detecting $N^+(1,1)$ and $N^+(1,0)$. The depth of modulation in the fragment yields during the rotational wave packet revival is partially limited by the non-collinear geometry of the pump probe overlap. It should be noted that the absolute size of the modulations means that dynamic alignment (alignment of the molecules during the probe pulse) cannot be overwhelmingly large, but at the same time, it is possible and even likely that some percentage of molecules within 5–10° of the ionization pulse polarization angle might be rotated towards the polarization.

3.2 Oxygen Alignment

In an effort to determine whether the polarization effects we saw were truly due to orbital effects, or were due to physical characteristics of our experimental chamber, we performed similar experiments in O_2, which has a very different highest occupied molecular orbital (HOMO) structure with four-lobed structure (π_g symmetry, antibonding), as compared to the HOMO structure of N_2 (σ_g symmetry, bonding) [6, 52]. When we again rotate only the ionization beam polarization, we find that the yields for O_2 ions behave very similarly to N_2. Figure 3.6 shows that the ion yields have an elongated structure, indicating enhanced yield at 0° between the pump and probe polarization beams. However, we should see the four-lobed structure in these ion yields, with a peak yield at $\sim 40°$ relative to the polarization angle. The reason we do not is that we are generating post-ionization alignment (PIA) [59]. PIA occurs when the ions continue to rotate to align with the laser polarization after the ionization pulse is off. This ion alignment overwhelms the neutral alignment that we hoped to see. PIA is more common with pulses which are long compared to the initial alignment time, and apparently our 30 fs pulses are long enough to cause significant PIA. PIA also makes it impossible to extract $P(\theta)$ values

---

[1] Because the N_2^{2+} is an intact parent ion, it has no partner with which to exchange momentum, and therefore is much less likely to miss the hole in the top plate of the TOF system.

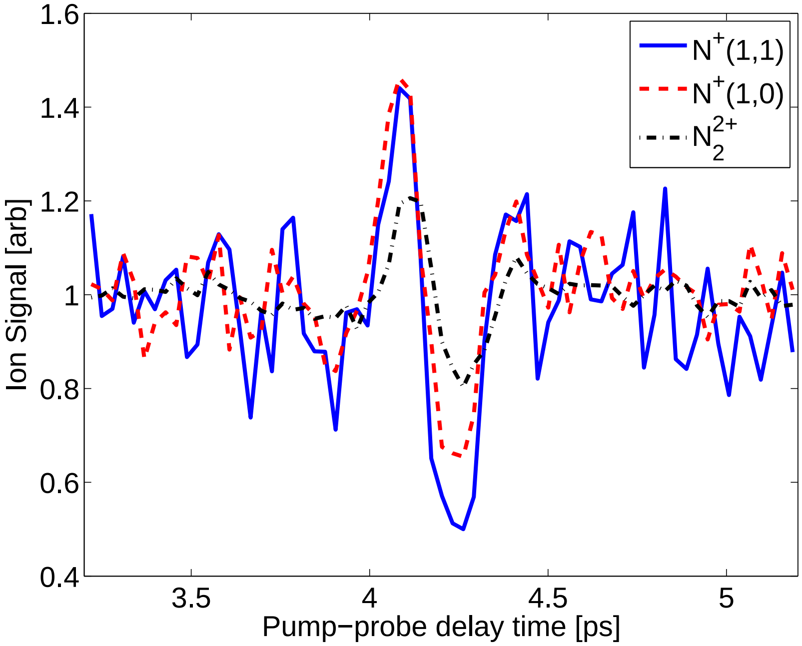

Figure 3.5: This pump-probe scan shows the half-revival structure at 4.2 ps. Both pump and probe beams were polarized parallel to the TOF axis. Note that revival amplitude varies depending on the particular fragment, but this is mostly due to dissociation effects - the nondissociative ions have no dissociation energy and thus can be collected even when they aren't aligned, whereas the dissociative ions miss the hole.

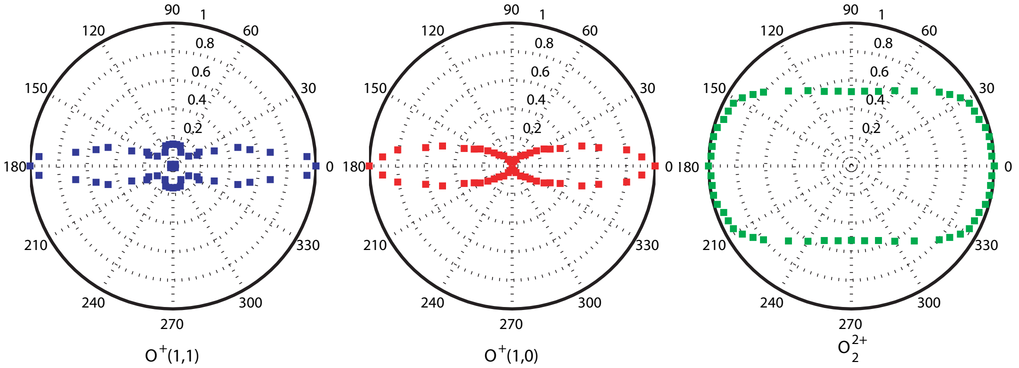

Figure 3.6: Polar plots of the O_2 ion yield (normalized) for only the ionization beam rotating. Angle is measured from the TOF axis. This is equivalent to single beam data with a slightly narrower detection function.

from the N_2 data.

3.3 Trifluoroacetone

Having confirmed that we could align molecules with the new chamber, we turned to larger molecules. 1,1,1-trifluoroacetone (CH_3COCF_3) is a halogenated molecule that had been used in previous control experiments in the lab [28, 44, 45]. Figure 3.7 shows a ball-and-stick model of trifluoroacetone (TFA). As mentioned above, we hoped that alignment would allow us to increase the degree of control over CF_3^+ production.

Initial rough estimates by a collaborator [60] showed that TFA should have a revival time of 140-250 ps, depending on which rotational axis is involved. Since a delay stage for such travel times would have to be at least 3.5 cm long to see the full revival[2], it would be very difficult to see multiple revivals. However, we hoped to see the initial revival. When an alignment pulse enters, the molecules require a small amount of time to initially rotate into alignment. For small molecules such as N_2 and O_2, this time is less than the width of our pulse, and thus any change in the yield is buried in the time zero signal. However, for TFA we expect this time to be on the order of 5-10 ps and therefore accessible with a 2.5 cm delay stage. This much longer initial alignment time also means that PIA should not be a problem.

---

[2] Specifically, $x = \frac{ct}{2}$, where c is the speed of light, t is the time delay required, and the factor of two is due to retroreflecting the beam.

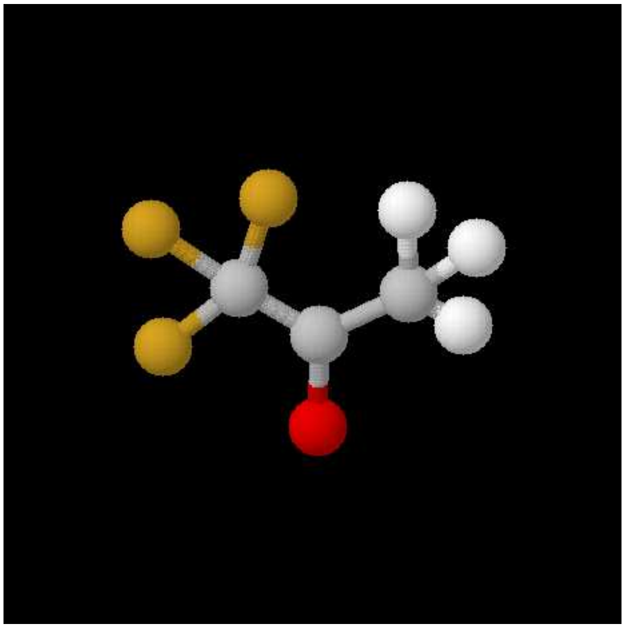

Figure 3.7: Ball-and-stick model for 1,1,1-trifluoroacetone, CH_3COCF_3.

Some pump-probe scans, such as the one in Figure 3.8, revealed signs of an initial alignment. However, these scans were not repeatable, so we could not confirm alignment in TFA. Possible reasons include the temperature of the molecular beam. If the temperature is not low enough, one cannot obtain good rotational coherence. Alternatively, the polarizabilities of TFA may not be suitable for alignment. TFA is a three-dimensional molecule, likely with three non-zero components to its polarizability tensor α. If $\alpha_{\parallel}$ is not strong relative to the two other components, achieving alignment with a linearly polarized beam would be difficult.

Fig. 3.8 shows a slow rise in ion yield after time zero that rises over ~25 ps and persists for at least 60 ps. The fast oscillations are likely a noise artifact from binning the data. This signal was present only in CF_3^+; CH_3CO^+ and CH_3^+ were level as a function of time delay. We used an elliptical alignment pulse with the major axis at 30° relative to the ionization pulse because structure calculations [60] indicate the presence of two axes with similar polarizability. Elliptical polarization is the only way to align along two axes with a single laser pulse. However, the difficulty in reproducing the 'alignment' signal, combined with the fact that it persists out to 60 ps or more, suggests that we have not created an aligned sample of TFA.

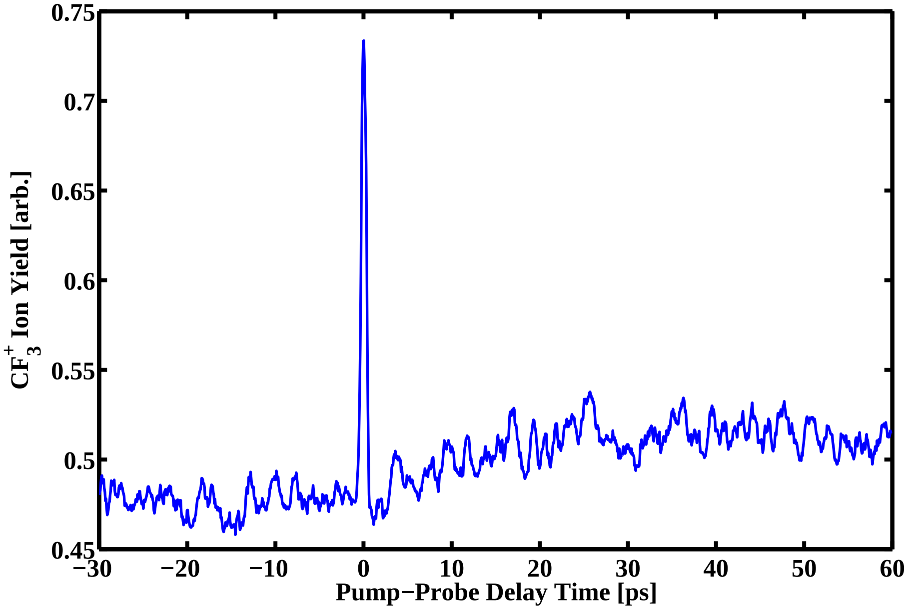

Figure 3.8: Pump-probe data for CF_3^+ from trifluoroacetone. The scan used an elliptically polarized alignment pulse with major axis 30° from the unshaped ionizing pulse.

3.4 Conclusion

We have demonstrated alignment in N_2 and O_2 molecules. For small molecules, our 30 fs pulse is long enough to cause post-ionization alignment, which limits our ability to resolve the orbital structure in these molecules. However, we can clearly resolve the temporal revival structures in such molecules, indicating the successful creation of a molecular beam. We also tried to create alignment in a large asymmetric molecule, trifluoroacetone (CH_3COCF_3), in order to enhance the control of CF_3^+ production. Future work includes adding a planned two-stage extraction field [61], which will enhance our TOF energy resolution for peaks with different kinetic energy.

Chapter 4

Halomethanes

Halomethanes are a family of molecules structurally similar to methane, CH_4, but with one or more of the hydrogens replaced by members of the halogen family (Group 17/old Group VIIA on the periodic table). This chapter discusses various work on halomethane molecules of the form CH_2XY, where $X,Y \in \{Br, Cl, I\}$. Because the hydrogen atoms are small by comparison with the much larger halogens, have only a single electron (which is bound), and stay relatively close to the carbon, a halomethane with two halogens is effectively a triatomic system (carbon plus the two halogen atoms). This quasi-triatomic nature of CH_2XY molecules has made them attractive prototypical molecules for studying and controlling unimolecular dissociation reactions (for examples in CH_2BrI and CH_2I_2, see [28, 62–74]). We choose the halomethane family of molecules for multiple reasons. These molecules have been studied extensively, partly due to their importance in atmospheric chemistry [67]; $CHBr_3$, CH_2Br_2, CH_2ClI, CH_2BrI, and CH_2I_2 are all produced in varying quantities by oceanic algae (for example, see [75, 76]), can provide a source of reactive halides which lead to ozone destruction, and thus are incorporated into global atmospheric models (such as [77]). We also study them because of our interest in control, and because they illustrate the importance of dynamic ionic resonances in dissociative ionization [24, 25]. As discussed earlier, small molecules such as halomethanes also have the advantage of calculable potential energy surfaces with a limited number of reaction coordinates. Figure 4.1 shows ball-and-stick models of the molecules under investigation, specifically CH_2I_2, CH_2ClI, CH_2Br_2, and CH_2BrI. CH_2Br_2 and CH_2I_2 are symmetric halomethanes of the form CH_2X_2, while CH_2BrI and CH_2ClI are asymmetric molecules, where $X \neq Y$.

Our original goal in investigating these molecules was to control the dissociation dynamics of the halomethanes using a genetic algorithm [78] to shape our laser pulses, as described in Chapter 2. In order to understand our con-

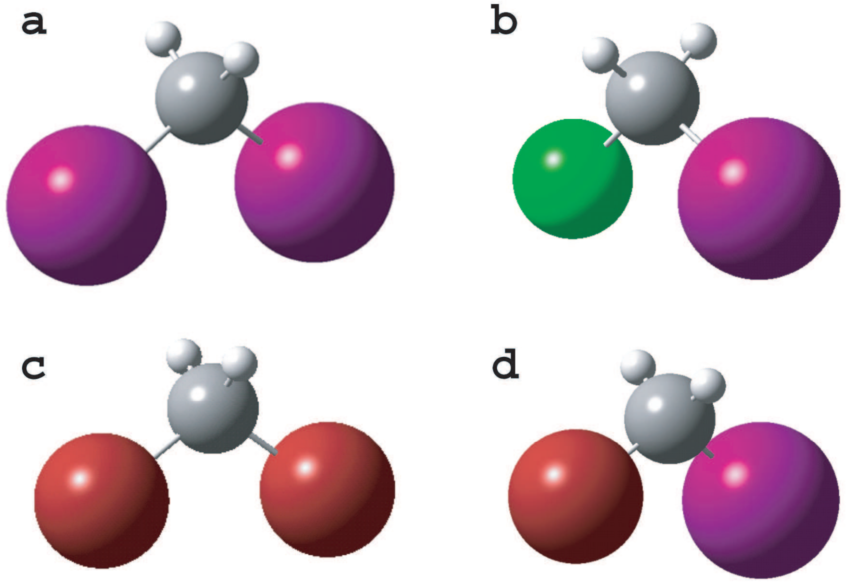

Figure 4.1: Ball-and-stick representations of the halomethanes under investigation: a) CH_2I_2 b) CH_2ClI c) CH_2Br_2 d) CH_2BrI.

trol results, we decided to systematically vary our laser pulse parameters in order to understand better both the dynamics inherent to the molecules and the strong-field-induced dynamics. For simplicity, all experiments presented in this chapter were performed in an older and less complicated chamber than the one described in Chapter 2. This chamber has only an effusive molecular source [33, 35] and thus no molecular cooling. We first performed pump-probe scans, varying the delay between two unshaped pulses. When this revealed interesting temporal structure, we varied other pulse parameters as well, in order to gain a more detailed picture of the dynamics. We also wanted to compare the experimental results with the results of *ab initio* molecular structure calculations, in hopes that the combination of calculation and theory would give us a more robust picture than either alone. For the calculations we turned to a collaborator, Dr. Tamás Rozgonyi of the Hungarian Academy of Sciences, and the calculations presented here are all his unless noted otherwise.

We start by presenting the experimental results on the halomethane family, beginning with the initial control experiments and moving on to experiments in which we vary the time delay between pulses, the chirp (duration), the polarization, and the energy of our laser pulses. The variations in ion yield as a function of time delay and pulse energy were key to developing an initial picture of the wave packet dynamics. We then continue with a discussion of the calculated potentials and the resulting dynamical wave packet calculations and finish with a discussion of the implied dynamics obtained from the combined calculated and experimental data.

4.1 Experimental Results

We started investigating halomethanes in an effort to control their dissociation. That is, we hoped that by shaping our laser pulse we could control the ratio of different ion fragments. Figure 4.2 compares the ion yields for a single transform- limited (TL) pulse, two TL pulses separated by 200 fs, and a TL pump pulse followed by a shaped probe pulse when applied to CH_2BrI. In the latter case, the GA [28, 33] was allowed to optimize the probe pulse in order to maximize the differential ion yield $CH_2I^+ - CH_2BrI^+$. The 200 fs delay was chosen to be sure that the two TL pulses (FWHM ~35 fs) would not overlap in time. The overall goal was preferentially to break the stronger C-Br bond while leaving the weaker C-I bond intact. We see that a single TL pulse creates a small amount of the CH_2I^+ daughter fragment, and a large amount of the parent ion. Adding a second TL pulse decreases the yield of the parent ion and increases the yield of the daughter ion. Shaping the second pulse has an even greater effect, such that we can increase the daughter ion yield by a factor of 2 over a single TL pulse.

The results of our control experiment seemed to imply a classic "pump-dump" scheme [79], where the first pulse pumps the system to an excited state, the system evolves on that state, and a later pulse dumps the system into a final, dissociative state. However, the optimal probe pulse generated by the GA was long and complex, as seen in Figure 4.3. In order to understand the details of the dissociation dynamics more completely, including which potential energy surfaces were involved, we measured the ion yields for several molecules and a wide variety of pulse parameters. TL pulses were used for all of the measurements below in which a specific pulse shape is not discussed, and all laser polarizations are perpendicular to the TOF axis unless a different polarization is mentioned.

Pump-probe measurements in the CH_2XY family of molecules result in oscillating parent and daughter ion yields as a function of pump-probe delay, as seen in the figures below. Figure 4.4 shows the pump-probe results for CH_2I_2; Figure 4.5 shows CH_2Br_2; Figure 4.6 shows CH_2BrI; and Figure 4.7 shows CH_2ClI. Pump pulse intensities were $\sim 7 \times 10^{13}$ W/cm^2, while probe pulses were weaker, $\sim 2 \times 10^{13}$ W/cm^2. The daughter ions that display strong modulations in their yield are all formed by the scission of a C-X bond: CH_2Br^+

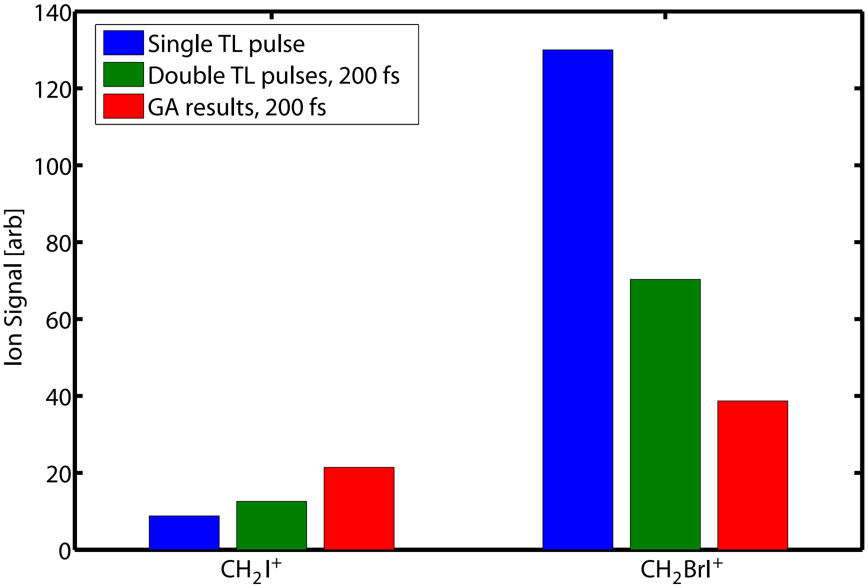

Figure 4.2: Results of a control experiment on CH_2BrI in pump-probe configuration. The genetic algorithm (GA) shaped the probe pulse, which arrived 200 fs after the pump pulse. The GA goal was to increase the differential yield of CH_2I^+ - CH_2BrI^+.

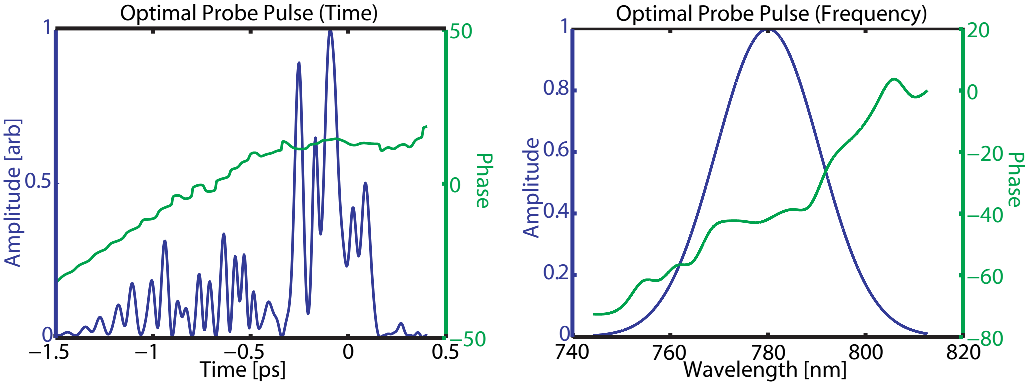

Figure 4.3: The shape of the optimal probe pulse which gives the CH_2BrI control results seen in Fig. 4.2. The intensity and phase of the pulse are shown as a function of time (left) and wavelength (right).

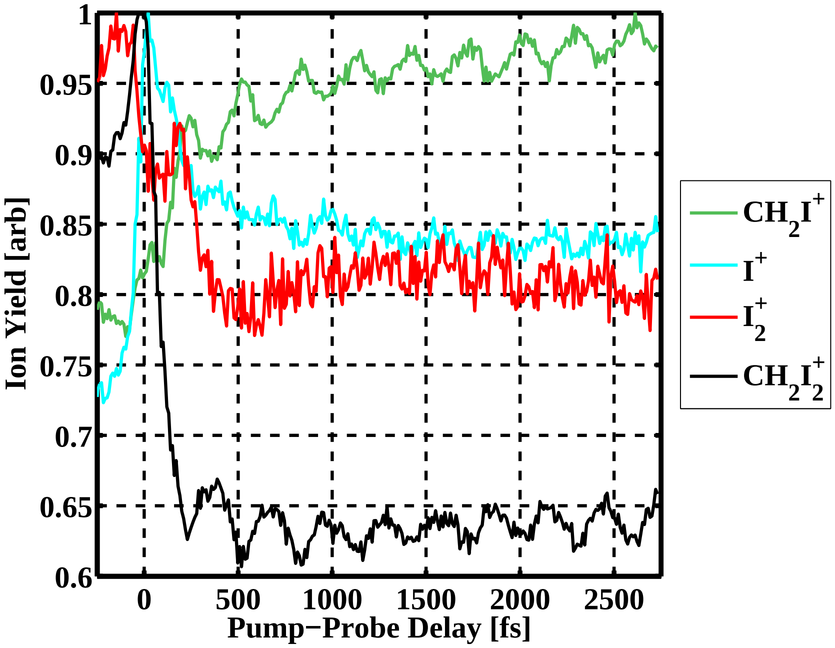

Figure 4.4: Pump-probe signals for $CH_2I_2^+$ and daughter ions. Note the formation of I_2^+ by concerted elimination.

from CH_2Br_2, CH_2I^+ from CH_2I_2, CH_2Br^+ from CH$_2$BrI, and CH_2Cl^+ from CH$_2$ClI. Thus, the modulations in these daughter ion yields are always π out of phase with their respective parent ion, as the daughter ions can only be created by breaking a bond of the parent ion. The sharp spikes and dips seen at time zero reflect the nonlinear results of two spatially and temporally overlapping pulses, and will be ignored.

CH_2I_2 ion yields, as seen in Fig. 4.4, show strong modulations at 114 cm^{-1}. Note that the CH_2I^+ yield is π out of phase with the parent ion $CH_2I_2^+$. The I_2^+ yield, although noisy due to low signal levels[1], is π out of phase with CH_2I^+ and thus in phase with $CH_2I_2^+$. The I^+ yield also displays modulations which are in phase with the parent. As the concerted elimination of I_2^+ from CH_2I_2 has already been discussed elsewhere [80], we mention it only briefly here.

Fig. 4.5 plots selected ion yields from CH_2Br_2 as a function of pump-probe delay. CH_2Br^+ and $CH_2Br_2^+$ show single frequency oscillations that are π out of phase, as discussed above. The Br^+ daughter ion displays no oscillatory behavior, only a long decay. Br_2^+ is noisy here, but at some pulse energies, we see

---

[1] The signal to noise level is worse for inherently small signals due to shot noise, which goes as $\sqrt{n}$, where n is the number of counts received, so that $\frac{signal}{noise} = \frac{n}{\sqrt{n}} = \sqrt{n}$.

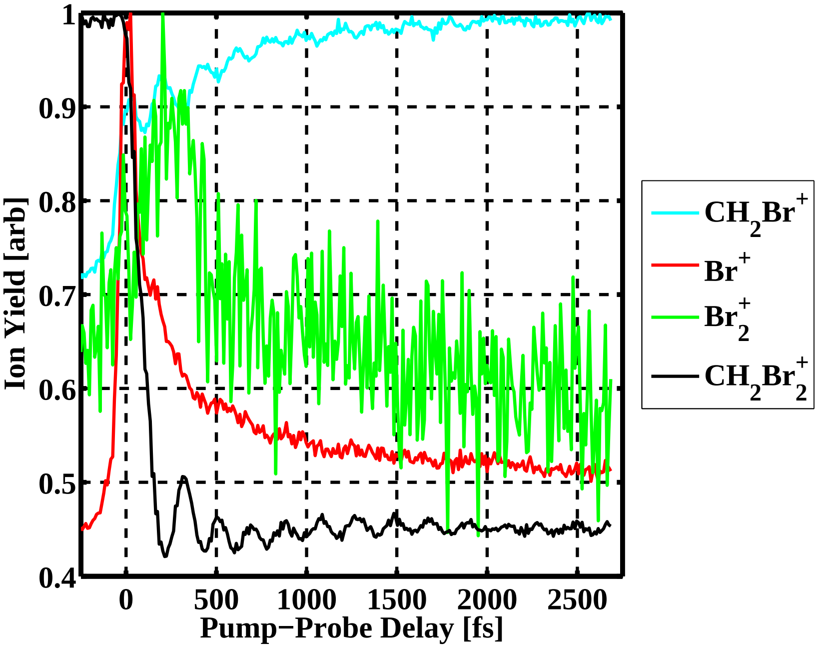

Figure 4.5: Pump-probe signals for $CH_2Br_2^+$ and daughter ions.

modulations similar to those in I_2^+, indicating a similar concerted elimination explanation is likely.

The asymmetry of CH_2BrI means that more daughter fragments are generated. Fig. 4.6 shows the four main daughter fragments Br^+, I^+, CH_2Br^+, and CH_2I^+, in addition to the parent ion CH_2BrI^+. Once again, we see strong modulations in the parent ion, mirrored in this case by CH_2Br^+. This time, the oscillations are formed by the beating of two frequencies with an apparent constant phase relationship, thus likely a fundamental and second harmonic. CH_2I^+ shows hints of oscillations, but nothing strong. I^+ shows oscillations at the fundamental frequency, which also appear to be π out of phase with that component of the CH_2BrI^+ oscillations.

Fig. 4.7 shows several ions in addition to the parent and major daughter ions. We see that in this case, temporal structure is not limited to a single daughter ion. CH_2ClI^+ displays the dual-frequency oscillation noted above, and the daughter fragment CH_2Cl^+ mirrors it with a π phase shift. However, CH_2I^+ and I^+ also display oscillating yields, predominantly at the fundamental frequency of 110 cm^{-1}. Given their similar shape, the I^+ oscillations are likely reflecting a further dissociative process, *i. e.*, $CH_2ClI + nh\nu \rightarrow CH_2ClI^+$, $CH_2ClI^+ + h\nu \rightarrow CH_2I^+ + Cl \rightarrow CH_2 + I^+ + Cl$. However, this is still under

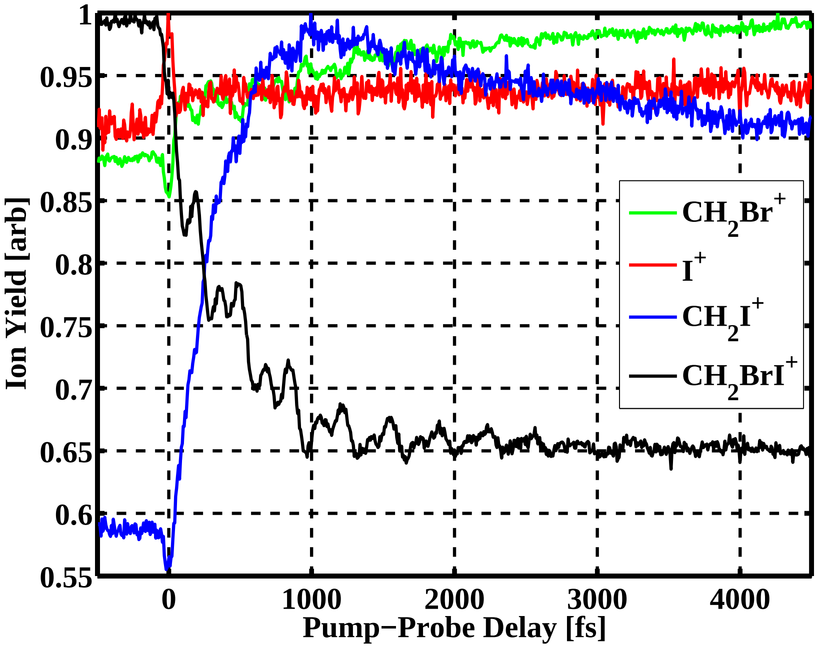

Figure 4.6: Pump-probe signals for CH_2BrI^+ and daughter ions.

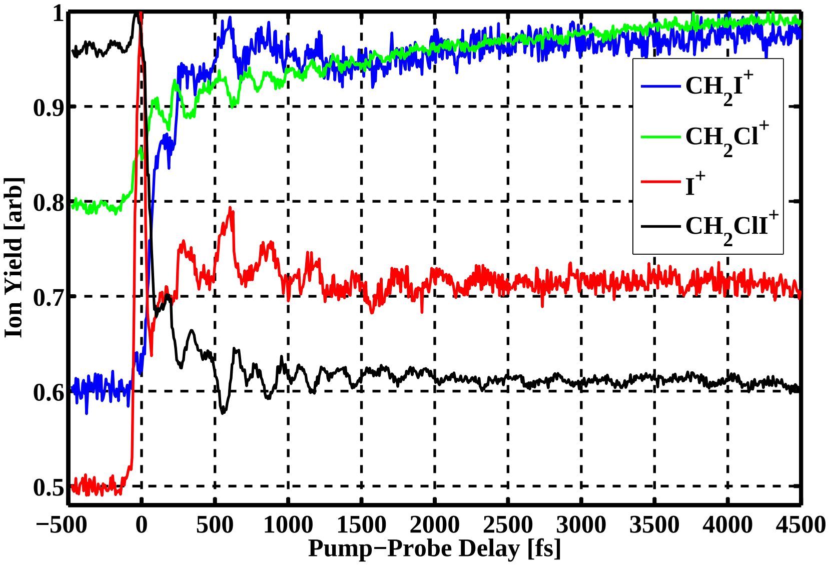

Figure 4.7: Pump-probe signals for CH_2ClI and daughter ions.

CH_2I_2		CH_2Br_2		CH_2BrI		CH_2ClI	
$CH_2I_2^+$	1	$CH_2Br_2^+$	1	CH_2BrI^+	1	CH_2ClI^+	1
CH_2I^+	1.44	CH_2Br^+	1.95	CH_2I^+	0.88	CH_2I^+	0.12
I^+	0.80	Br^+	0.68	CH_2Br^+	2.50	CH_2Cl^+	2.32
I_2^+	0.14	Br_2^+	0.02	I^+	2.76	I^+	0.46

Table 4.1: Halomethane maximum ion yields from Figs. 4.4–4.7, normalized to the maximum of the parent ion for the relevant molecule.

investigation, as discussed below.

Figs. 4.4–4.7 display ion yields that have each been normalized to their own maxima. For reference, Table 4.1 presents the maximum yields for each ion produced by a given molecule, normalized to the maximum of the parent ion.

If we compare the parent ion yields for all 4 molecules, as in Figure 4.8, we see that both CH_2BrI^+ and CH_2ClI^+ show oscillations at two frequencies, as determined by Fourier transform. In contrast, in the symmetric molecules CH_2I_2 and CH_2Br_2, the oscillations are predominantly at a single frequency, 114 cm^{-1} and 168 cm^{-1}, respectively. For the two-frequency oscillations, one frequency is the second harmonic of the other. Specifically, the frequencies are 94 ± 4 cm^{-1} and 196 ± 4 cm^{-1} for CH_2BrI^+, and 110 ± 4 cm^{-1} and 227 ± 4 cm^{-1} for CH_2ClI^+. The fundamental frequencies match published measurements and calculations for ionic vibrational modes [81, 82], as will be discussed later. Figure 4.9 shows the Fourier transform data for the curves in Fig. 4.8. The frequencies given above come from similar Fourier transforms obtained over a range of probe pulse energies.

Other less obvious features characterize these pump probe plots. In all cases, the average parent ion yield for a strong pulse followed by a weak pulse (positive time delay in the figures) is much less than the yield for a weak pulse followed by a strong one (negative time delay). Because the weak pulse has too little energy to create ions by itself, this indicates that a weak probe depletes the yield of parent ions created by a strong pump. However, this depletion is not instantaneous; a careful examination of the parent ion yields reveals a "turn-on" time (roughly the time to go from 90% to 10% of the signal level in the parent ion, or the reverse for the daughter ion). This turn-on time is fast in CH_2I_2 (<200 fs), moderately fast in CH_2Br_2 (∼200 fs) and CH_2ClI (∼300 fs), and much slower in CH_2BrI (∼1000 fs). Because the clearest structure is revealed in the parent ion and the mirroring daughter fragment (CH_2I^+ for CH_2I_2; CH_2Br^+ for CH_2Br_2; CH_2Br^+ for CH_2BrI; and CH_2Cl^+ for CH_2ClI),

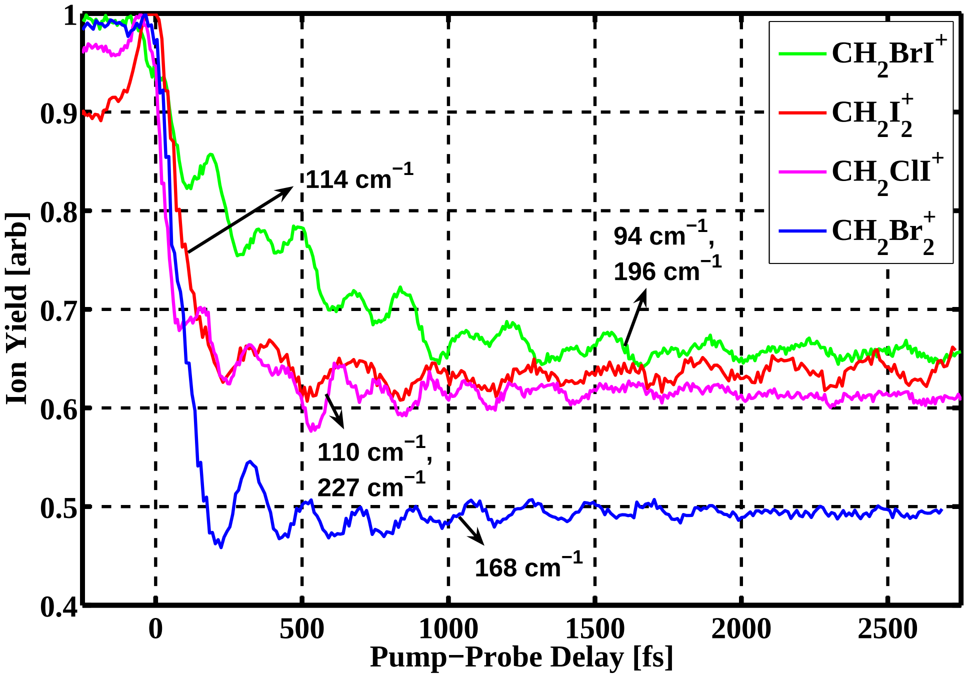

Figure 4.8: Pump-probe signals for parent ions from CH_2Br_2, CH_2I_2, CH_2BrI, and CH_2ClI. Note that there is predominantly one frequency present in the $CH_2Br_2^+$ and $CH_2I_2^+$ signals, but there are two frequencies present for the CH_2BrI^+ and CH_2ClI^+ signals.

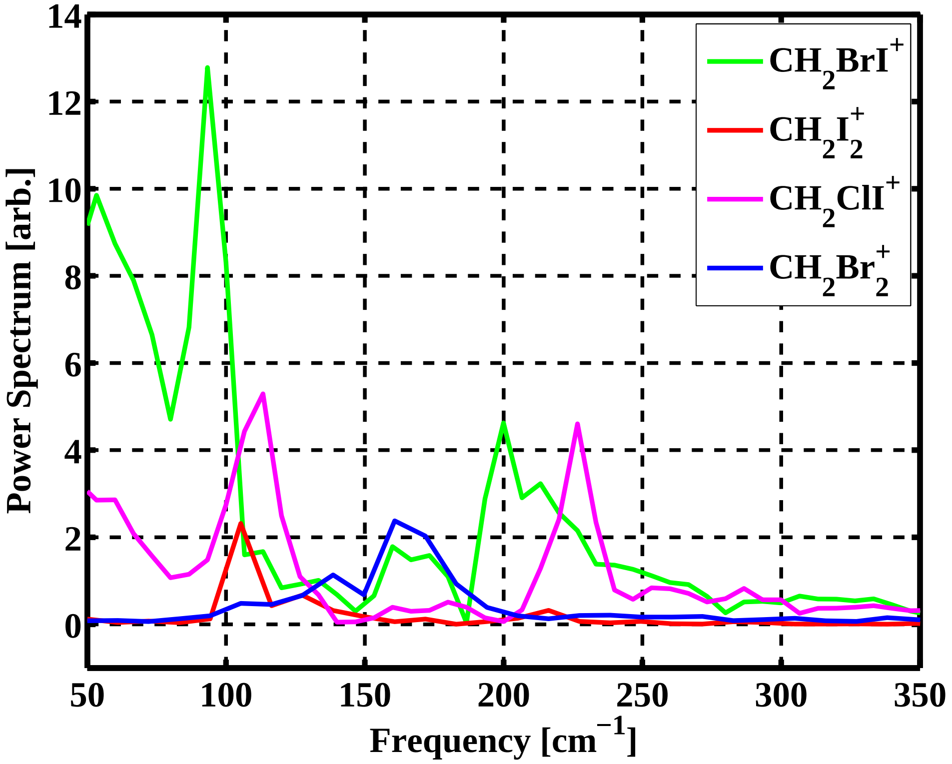

Figure 4.9: Fourier transforms for pump-probe yields of parent ions from CH_2Br_2, CH_2I_2, CH_2BrI, and CH_2ClI. Note that there is predominantly one frequency present in the $CH_2Br_2^+$ and $CH_2I_2^+$ signals, but there are two frequencies present for the CH_2BrI^+ and CH_2ClI^+ signals.

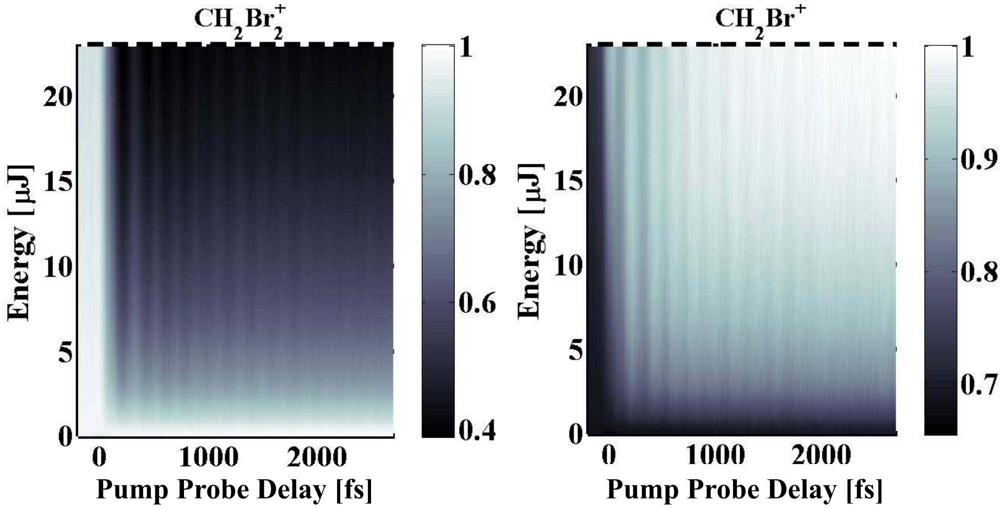

Figure 4.10: $CH_2Br_2^+$ yield (left) and CH_2Br^+ yield (right) as a function of pump-probe delay and probe pulse energy (intensity). The x-axis is the pump-probe delay time and the y-axis is the energy of the weaker probe pulse (which comes second for all positive time delays). The shading in both cases is arbitrary and represents the appropriate ion yield.

we will focus mainly on the parent ions for the remainder of the dynamics discussion.

The oscillations of our pump probe plots are not confined to a specific pulse energy (intensity), as a simultaneous scan of pump-probe delay and probe pulse energy shows. Figure 4.10 shows such a two-dimensional scan. We see that the parent ion oscillations (left side) persist at many probe energies. The CH_2Br^+ daughter ion oscillations (right side) are also clearly visible over a range of probe energies. Moreover, something interesting appears: as the probe pulse energy increases, the average yield of the parent ion decreases. This feature is common to all of the halomethanes, so long as the probe pulse is weak enough that it cannot create its own ions.

Figure 4.11 displays one-dimensional cuts from Fig. 4.10, highlighting the ion yield as a function of probe pulse energy for several different time delays. The parent ion decrease starts immediately at 0 μJ of probe energy, as seen in Fig. 4.11a. While the parent ion yield drops with increasing probe energy, the daughter ion yield rises, again, starting immediately from 0 μJ of probe energy (Fig. 4.11b. This nonzero slope at 0 μJ implies a linear molecular response to the probe pulse at low energies, which in turn indicates a single-photon

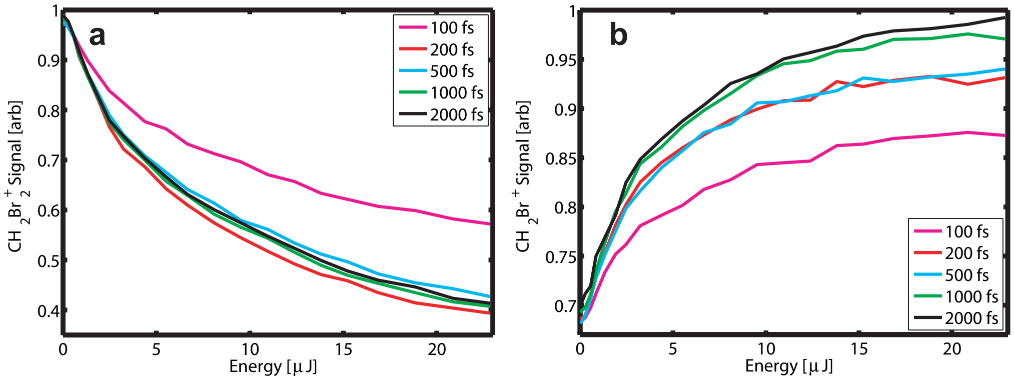

Figure 4.11: Ion yield as a function of probe energy at different pump-probe delays for a) $CH_2Br_2^+$ and b) CH_2Br^+. These are one-dimensional cuts along the energy axis from Fig. 4.10. Note the nonzero slope at 0 μJ in both ion yields, indicating a single-photon transition.

transition.

Clearly, the decrease in parent ion yield/increase in daughter ion yield is a two-pulse effect, as a scan of pulse energies with a single pulse shows the expected monotonic increase in yield for all ions. Figure 4.12 shows the yield for several ions visible in the dissociation of CH_2Br_2, with both absolute (Fig. 4.12a) and relative (Fig. 4.12b) ion yield scaling. H_2O^+, which has a relatively high ionization potential of 12.6 eV [40], is shown for comparison[2]. The parent ion CH_2Br_2 appears at low energies ($\sim$ 20 μJ), while H_2O^+ appears at higher energies $\sim$ 50 μJ), agreeing with their relative ionization energies of 10.4 eV and 12.6 eV, respectively. Br^+ also appears at higher energies ($\sim$ 40 μJ), indicating that it takes more energy to create, while CH_2Br^+ and Br_2^+ appear at roughly the same energies ($\sim$ 20-30 μJ) as the parent ion. Fig. 4.12b shows the relative size of the ion yields (integrated TOFMS peak areas) as a function of energy, showing a large amount of the daughter ion CH_2Br^+. Some of the ion yields, including $CH_2Br_2^+$, are starting to level off at very high energies, indicating saturation behavior (there are no more un-ionized molecules within the focus of the beam).

Similar single pulse energy scan results for CH_2I_2 are shown in Figure 4.13. Again, we see that the ion yields monotonically increase with pulse energy, with $CH_2I_2^+$, CH_2I^+, and I_2^+ all appearing ($\sim$ 10 μJ) and saturating ($\sim$ 70 μJ) at lower energies than I^+ ($\sim$ 20 μJ and $>$ 120 μJ, respectively). CH_2I^+ and

---

[2] H_2O^+ appears in our chamber due to background gas pressures, as does N_2^+ and O_2^+. As described in Ch. 2, we use these signals to pinpoint our absolute time delay.

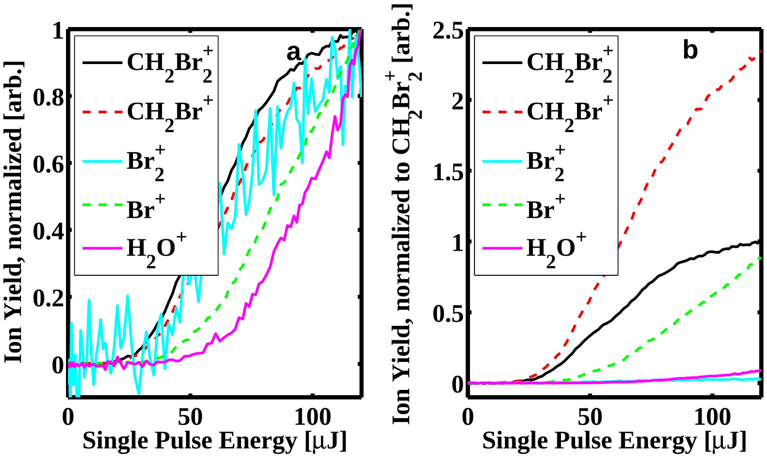

Figure 4.12: Ion yield versus single pulse energy for several ions from CH_2Br_2. a) Ion yields normalized to their own maxima. b) Ion yields normalized to the parent ion yield, for comparison. Fragments with a lower ionization energy, such as $CH_2Br_2^+$, appear and saturate at lower energies than fragments which require more energy to create, such as Br^+ or H_2O^+ (a molecule with high ionization potential, shown for comparison). Br_2^+ yields are noisy due to small absolute signal levels, but they follow the same monotonic behavior.

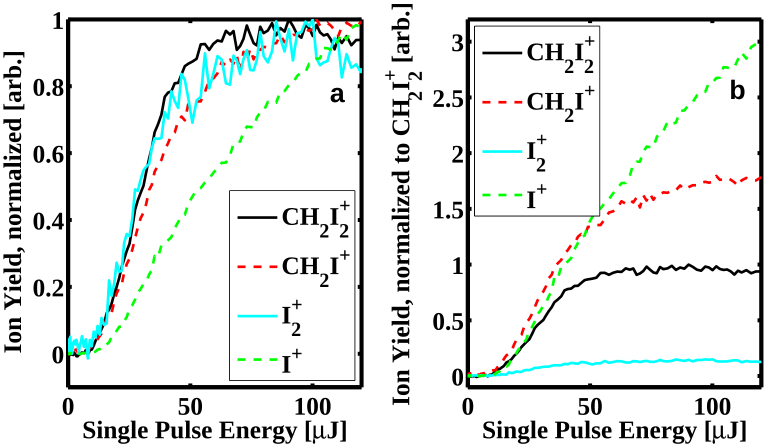

Figure 4.13: Ion yield versus single pulse energy for several ions from CH_2I_2. a) Ion yields normalized to their own maxima. b) Ion yields normalized to the parent ion yield, for comparison. Fragments with a lower ionization energy, such as $CH_2I_2^+$, appear and saturate at lower energies than fragments which require more energy to create, such as I^+. I_2^+ yields are noisy due to small absolute signal levels, but they follow the same monotonic behavior.

I^+ also have larger absolute yields than $CH_2I_2^+$ for all energies.

Figure 4.14 shows single pulse energy scans for CH_2BrI. In contrast with the symmetric molecules, all of the CH_2BrI ions saturate at much larger energies (> 120 μJ) than most of the CH_2Br_2 ions or the CH_2I_2 ions. The daughter ion CH_2Br^+ has a larger absolute yield than the parent ion CH_2BrI^+, and most of the ions (except Br^+) turn on at about the same energy (~ 40 μJ), which is higher than many of the turn-on energies in the symmetric molecules.

Figure 4.15 shows the CH_2ClI single pulse energy scan results. Once more, we see that the major daughter fragment (CH_2Cl^+) has a higher absolute yield than the parent ion (CH_2ClI^+), while CH_2I^+, Cl^+, and I^+ all have small yields relative to the parent. Similarly to the CH_2BrI case, all of the ions turn on at higher energies (~ 40 μJ) than in the symmetric molecules.

Given these single-pulse ion yields, the combination of daughter ion increase and parent ion decrease with increasing probe pulse energy in Fig. 4.11 strongly implies that we are looking at a resonant transfer from a bound parent ionic state to a dissociative state. The nonzero slope at 0 μJ probe energy implies a single photon resonance, and the temporal oscillations in yield suggest a bound state. The fact that it is the parent ion yield which is depleted implies that we must be transferring oscillating wave function out of a bound

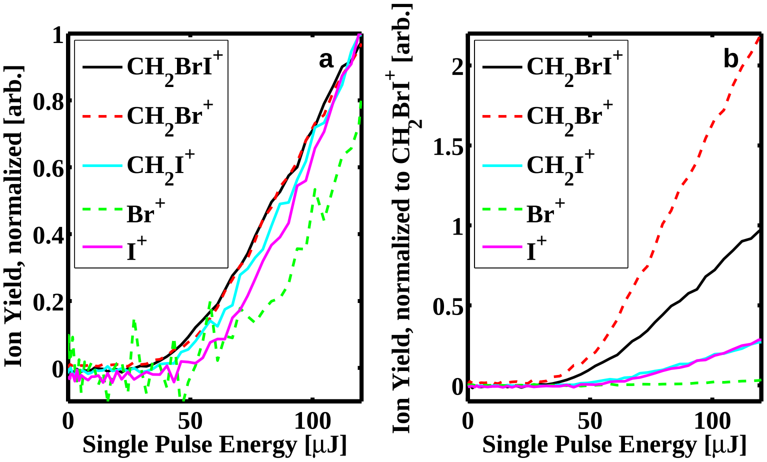

Figure 4.14: Ion yield versus single pulse energy for several ions from CH_2BrI. a) Ion yields normalized to their own maxima. b) Ion yields normalized to the parent ion yield, for comparison. Fragments with a lower ionization energy, such as CH_2BrI^+, appear and saturate at lower energies than fragments which require more energy to create, such as Br^+.

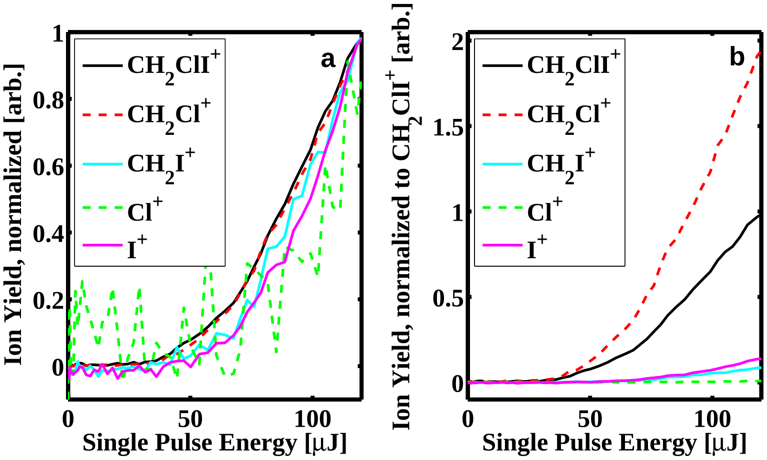

Figure 4.15: Ion yield versus single pulse energy for several ions from CH_2ClI. a) Ion yields normalized to their own maxima. b) Ion yields normalized to the parent ion yield, for comparison. Fragments with a lower ionization energy, such as CH_2ClI^+, appear and saturate at lower energies than fragments which require more energy to create, such as Cl^+.

parent ionic state.

Our experimental measurements support the following general picture of the dynamics, which is justified by detailed calculations discussed in Section 4.2. Figure 4.16 shows a cartoon picture of two-dimensional potential energy surfaces (PESs) relevant to ionization followed by dissociation in the halomethanes considered here. The molecule first undergoes tunnel ionization [11, 83**?**], which takes it from the ground state of the neutral (lowest state in the figure) to the ground ionic state (middle curve in the figure) at the location of the lower state equilibrium ($\mathrm{FC}_{\mathrm{pump}}$, for the Franck-Condon location of the pump pulse). As the neutral ground state and ionic ground state do not have the same equilibrium position, the vertical ionization process leads to the launch of a vibrational wave packet in the ground ionic state. While this wave packet is in principle multidimensional (*i. e.*, displacement along multiple coordinates), our calculations and measurements indicate that the displacement along one coordinate is significantly larger than along others, and we therefore consider the displacement primarily along one coordinate (x-axis in the figure). The wave packet oscillates along this dimension. At some x-location there is a resonance to an excited ionic state. When the wave packet on the bound ionic state passes through this single-photon (~ 1.58 eV) resonance, population in the bound ionic state may be transferred efficiently to the uppermost state, where it has enough energy to ride out over the barrier leading to fragmentation (along the y-coordinate). If the resonance location $\mathrm{FC}_{\mathrm{probe}}$ (for the Franck-Condon location of the probe pulse) is somewhere in the middle of the bound ionic potential, then the transfer can occur twice per oscillation. If the resonance location is not exactly in the middle, or the transfer efficiency is not the same for left-going and right-going wave packets, then the resulting transfer will have components at both the fundamental frequency of the potential and at its second harmonic. The lowest state in Fig. 4.16 corresponds to the neutral ground state of the molecule, while the intermediate state is a bound ionic PES. The highest state represents a dissociative ionic state (or a bound state coupled to dissociative states) whose separation from the bound ionic state for a particular x-coordinate is resonant in the near-infrared (~ 1.58 e V). This picture will become more detailed below.

The cartoon picture may help us understand some differences among the various halomethanes. For instance, in the pump probe scans for asymmetric molecules (Figs. 4.6 and 4.7), the resonant transfer takes place twice per oscillation in the well, but it is not equally transferred both times (big dip-little dip pattern). Calculations (discussed further in Section 4.2) indicate this temporal asymmetry varies with probe pulse energy, so we decided to investigate it experimentally. Figure 4.17 shows the results if we take pump probe scans

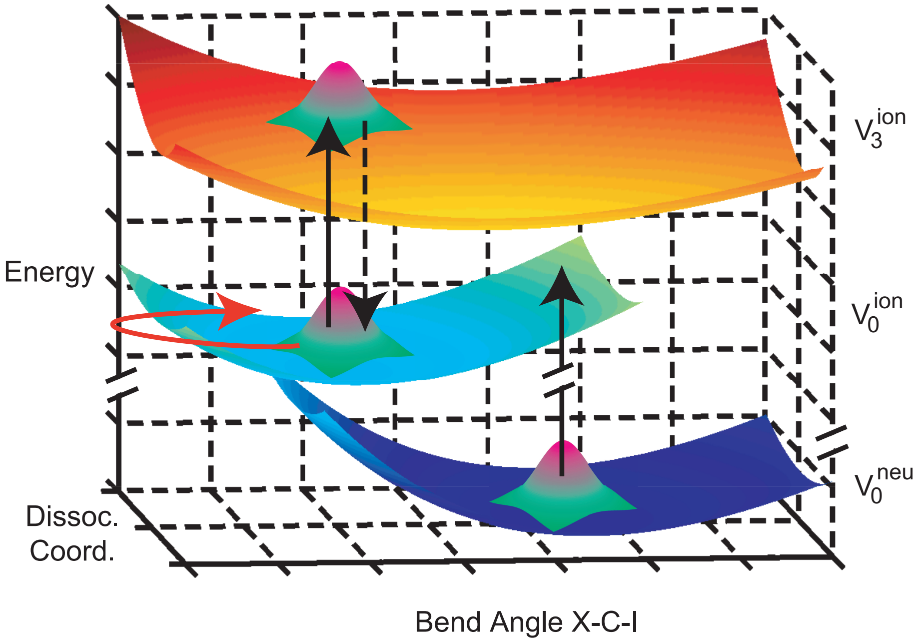

Figure 4.16: A cartoon of three important potential energy surfaces in the CH_2XI family of molecules: the ground neutral state V_0^{neu}, the ground ionic state V_0^{ion} (reached via tunnel ionization - note the broken vertical axis), and an excited ionic state V_3^{ion}. A wave packet launched high on the V_3^{ion} surface can dissociate along the C-I bond.

at a variety of probe pulse energies for all four molecules. These are equivalent to one-dimensional cuts along the time axis in data sets like the one displayed in Fig. 4.10a. As we increase the probe pulse energy (move in the negative y direction on the plots), the average parent ion yield decreases, as noted above. However, the character of the oscillations also changes. This is especially noticeable in the asymmetric molecules CH_2BrI and CH_2ClI (Fig. 4.17c, d). At low energies, all the peaks and dips in the oscillations are about the same size (in the Fourier domain, this corresponds to the second harmonic oscillations dominating the signal). As the probe pulse energy increases, the symmetry is broken, creating the big dip/little dip pattern (in the Fourier domain, this means the fundamental:second harmonic ratio is increasing). If the parent depletion occurs twice per cycle because FC_{probe} is near the middle of the well, then this means that at low energies, left-going wave packets and right-going wave packets are equally depleted. However, at higher energies, the asymmetry of the dip pattern means that left-going and right-going wave packets are not equally depleted by the probe. There are some hints of similar behavior in the symmetric molecules; for example, the $CH_2I_2^+$ curve at 2.5 μJ has somewhat “flat-topped” peaks, while at higher energies, the curves more closely resemble a pure sine wave at the fundamental frequency of 114 cm^{-1}. This left-right wave packet momentum asymmetry will be discussed in more detail in Section 4.3.

The cartoon picture given above implies the changing position of the wave packet in a potential may affect the possibility of resonant transfer to a dissociative state. When there is strong coupling between two potentials combined with wave packet motion, we expect the detailed properties of the electric field interacting with the system to play an important role in the efficiency of the transfer. Thus, it may be possible to tune the laser pulse characteristics to enhance the transfer. Using our pulse shaper, we can apply quadratic spectral phase to the probe pulse, thus chirping it out in both positive (low frequencies arrive before high frequencies) and negative (high frequencies arrive before low frequencies) directions. We can also programmatically control the energy in the probe pulse. For certain probe energies, the degree of chirp strongly impacts the ion yields, as seen in Figures 4.18, which shows ion yields as a function of probe pulse chirp (x-axis) and energy. We see that at moderate probe pulse energies, a chirped pulse can deplete the parent relative to a TL pulse. Similarly, a chirped pulse increases the daughter ion yield relative to the parent. This is **not** due to the decrease in intensity that accompanies increased chirp magnitude at a constant pulse energy; if it were purely an intensity effect, lower intensities should result in increased parent ion yields, as seen in the pump-probe energy scans above (Fig. 4.10).

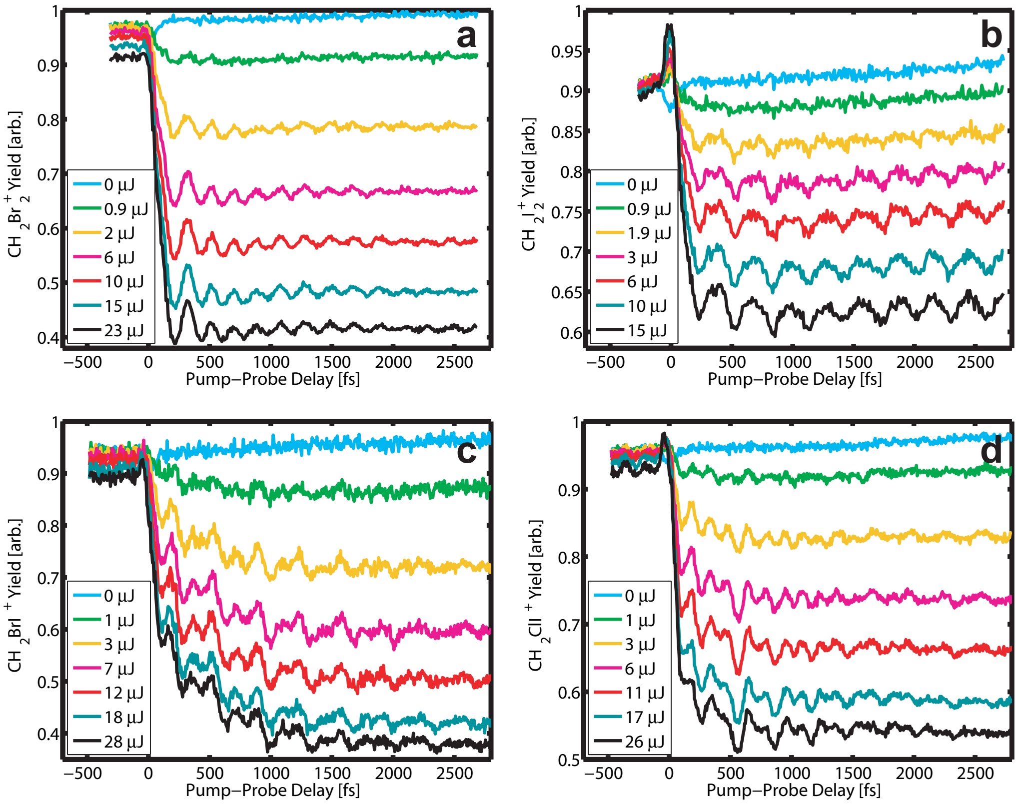

Figure 4.17: Pump-probe scans as a function of probe pulse energy for a) CH_2Br_2 b) CH_2I_2 c) CH_2BrI and d) CH_2ClI. Probe pulse energy increases monotonically as the mean yield at positive time delay decreases on all four plots.

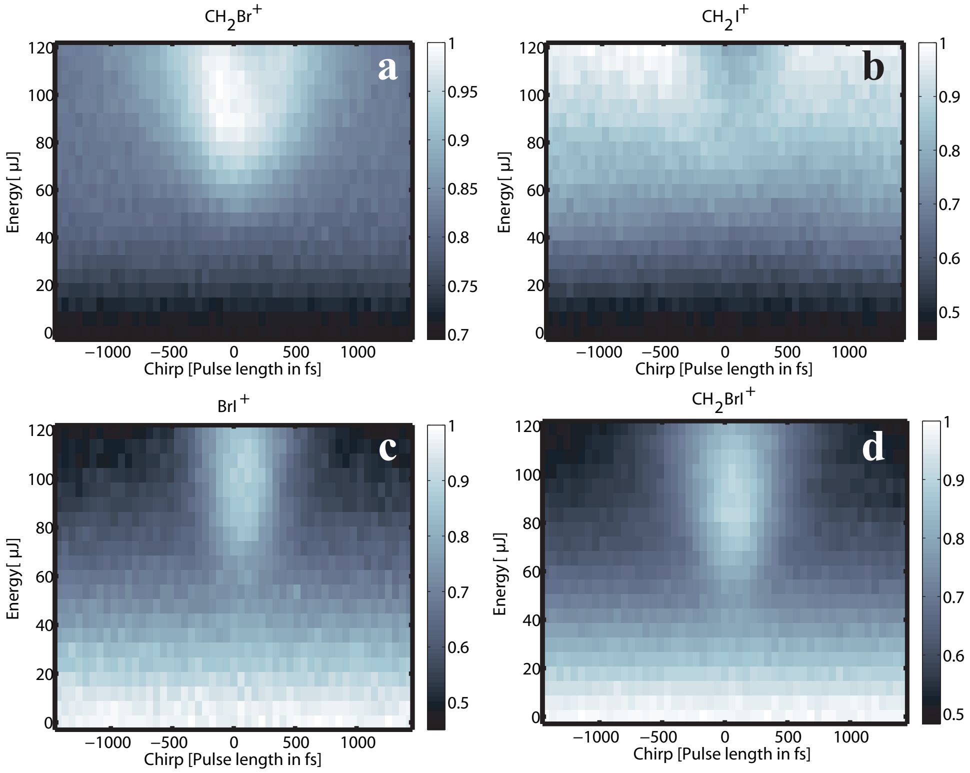

Figure 4.18: Chirp energy scans for a) CH_2Br^+ b) CH_2I^+ c) BrI^+ d) CH_2BrI^+, all from CH_2BrI. The horizontal axis is chirp, labeled as the pulse width (with negative width indicating negative chirp). The vertical axis is energy. The color axis is arbitrary for all ions. There was a 2000 fs delay between pump and probe pulses.

One possible explanation involves the presence of additional potential energy surfaces beyond the three shown in Fig. 4.16. As we will discuss below, the presence of multiple ion fragments with roughly the same turn-on energy, as seen in Figs. 4.12-4.15, indicates that our pump pulse promotes wave function onto multiple states. In particular, we likely excite V_1^{ion}, the first excited ionic state. Wave function may slowly leak onto V_0^{ion}, meaning that the total wave function on V_0^{ion} has the shape of a narrow peak on top of a broad base. A chirped pulse is on for a longer time than a TL pulse of equivalent energy, and so has time to promote more of the broad base of the wavefunction through the resonance. The lower parent ion yields and increased daughter ion yields for chirped pulses are consistent with this picture of a chirped pulse capturing more of the wave function.

The laser polarization can also affect ionization and dissociation; specifically, the alignment dependence of the ionization and dissociation can help to identify the amplitudes of the states involved and test the control mechanism. Although the halomethane experiments are performed at room temperature, and thus we cannot align the molecules to any great degree using non-adiabatic laser alignment, the molecular dynamics may still depend on the relative alignment of the molecule and the laser polarization. For instance, our pump pulse may differentially ionize molecules that happen to be aligned with the pump polarization, so that a non-uniformly distributed set of orientations is available to the probe pulse for dissociation. If alignment of the molecular orbitals makes a difference in ionization and/or dissociation, we would expect to see differences in the pump probe scans with different probe pulse polarizations (relative to the pump pulse polarization). Ionization and dissociation signals that varied with laser polarization might also tell us something about the orbital structure of the molecules. One example is that ionization from the highest occupied molecular orbital (HOMO) might preferentially lead to one subsequent dissociation pattern (such as CH_2X^+ + Y), while ionization from the HOMO-1 (the second highest occupied molecular orbital) might lead to a different dissociation (such as CH_2Y^+ + X). Figures 4.19 and 4.20 present the pump probe scans at different polarizations for the two symmetric parent ions $CH_2Br_2^+$ and $CH_2I_2^+$, respectively. We can see subtle differences in the shape of the curves.

For both $CH_2Br_2^+$ and $CH_2I_2^+$, the amplitude of the drop in yield from before time zero to the average yield at long time delays (1500–2000 fs) is the same to within $< 2\%$ for parallel and perpendicular laser polarizations. The amplitude and shape of the oscillations at long time delays is also nearly identical. However, at short time delays ($\lesssim$500 fs after time zero), the oscillations are as much as 15-20% larger for a perpendicular probe polarization as

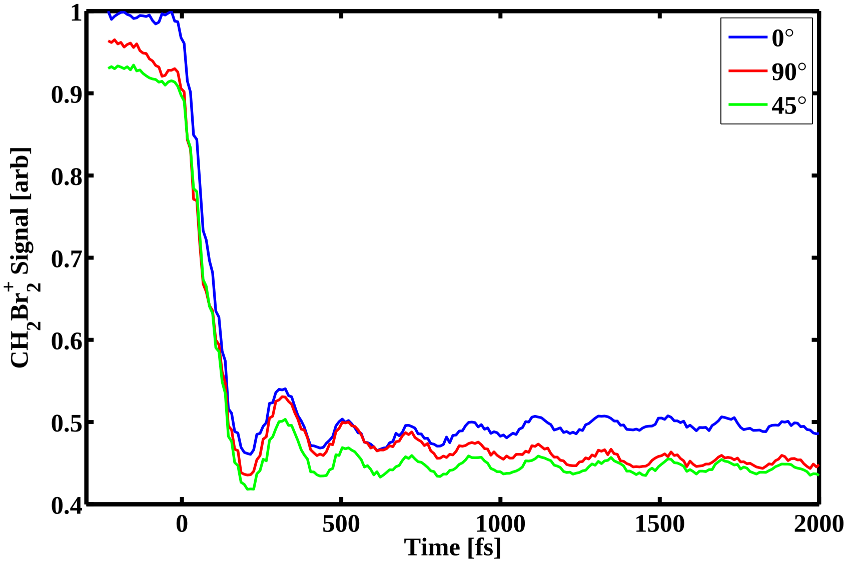

Figure 4.19: Pump-probe scans for parent ion $CH_2Br_2^+$ at different probe pulse polarizations. Polarization is measured relative to the pump pulse polarization, which is horizontal (perpendicular to the TOF path). The slight offset is due to the gradual decrease in chamber pressure between scans.

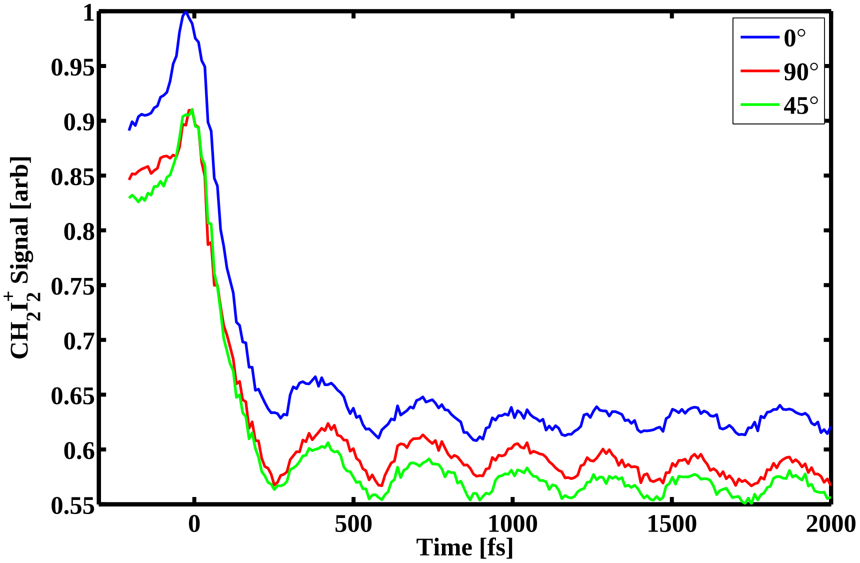

Figure 4.20: Pump-probe scans for parent ion $CH_2I_2^+$ at different probe pulse polarizations.

compared to a parallel one. A quick estimate allows us to see whether it is reasonable to attribute this to selective alignment dependent ionization from a randomly oriented sample. The halomethane molecules are not cooled in a molecular beam, so we do not expect the clean rotational revivals we saw in Chapter 3. However, the pump pulse could still preferentially select a subset of molecules which are aligned with the laser for ionization. These molecules would then rotate out of alignment after some time delay and eventually dephase. In N_2, the time to go from a fully aligned ensemble at the peak of a revival to a fully anti-aligned one at the dip of a revival (90° rotation time) is ∼100 fs. Each atom has a mass of 14 amu, and the bond length is 1.09 Å, so the resulting moment of inertia is

$$I = 2mR^2 = 2 * (14\,\text{amu}) * (0.54\,\text{Å})^2 = 8.16\,\text{amu} * \text{Å}^2.$$

For CH_2I_2, although we do not know the rotation axes, we know the equilibrium structure, and we can choose arbitrary rotation axes to compare the resulting 90° rotation times. The calculated equilibrium structure in CH_2I_2 gives a C-I distance of 2.15 Å and an I-C-I angle of 116°. We will consider CH_2I_2 to be a triatomic for this estimate, with a CH_2 mass of 14 amu. For rotation of one I atom about the axis formed by the other C-I bond, we have

$$I = mR^2 = (127\,\text{amu}) * (2.15\,\text{Å} * \cos(26°))^2 = 474\,\text{amu} * \text{Å}^2.$$

Given that the molecules are rotationally torqued by the same laser, we expect $I \propto T^2$, where T is the period of rotation, and of course the 90° rotation time $t \propto T$. So,

$$t_{\mathrm{CH_2I_2}} = t_{\mathrm{N_2}} * \sqrt{\frac{I_{\mathrm{CH_2I_2}}}{I_{\mathrm{N_2}}}}.$$

For the values above, then, we have a 90° rotation time $t_{CH_2I_2} = 760$ fs.

If we instead suppose that the rotation is of $\mathrm{CH_2}$ about the axis formed by the two I atoms, we have

$$I = mR^2 = (14\,\text{amu}) * (1.14\,\text{Å})^2 = 18.2\,\text{amu} * \text{Å}^2,$$

giving $t_{\mathrm{CH_2I_2}} = 150$ fs. This is considerably shorter, and thus less likely to be an explanation for the oscillation size effects we see. However, the longer $t_{\mathrm{CH_2I_2}}$ of 760 fs is quantitatively similar to the time range in which the oscillations of perpendicular probe polarization are larger than the oscillations for parallel polarization. We will explain further how polarization is related to molecular structure in Section 4.3, after we have discussed the potential energy surfaces in more detail.

Shape changes as a function of probe pulse polarization are not limited to the symmetric molecules. We also see a variation in the shape of the curve with polarization for $\mathrm{CH_2BrI}$, as seen in Figure 4.21.

As in the symmetric molecules, the size of the overall drop in ion yield from before time zero to long time delays is the same for both parallel and perpendicular probe pulse polarizations. If we measure the size of the oscillations, we see that again, some oscillations are larger ($\sim 20\%$) for perpendicular probe polarizations at times $\lesssim 1000$ fs after time zero. Using the equilibrium coordinates given in Appendix A, we find a 90° rotation time of $t_{\mathrm{CH_2BrI}} = 790$ fs for rotation of I about the C-Br axis, and a time of 560 fs for rotation of Br about the C-I axis, so again, these times indicate that rotational motion is a quantitatively reasonable explanation for the change in oscillation size with probe pulse polarization.

4.2 Calculations

Electronic structure and wave packet propagation calculations are an essential part of interpreting our experimental results. We relied heavily on the

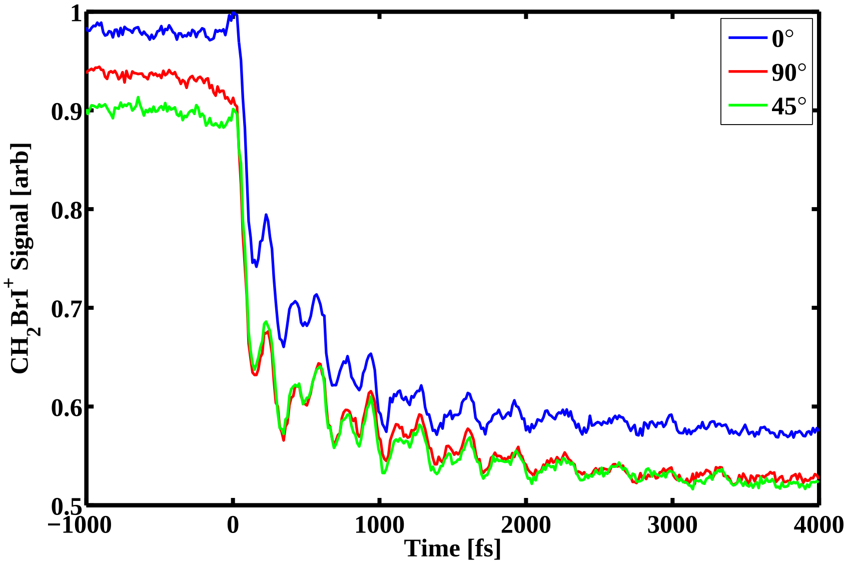

Figure 4.21: Pump-probe scans for parent ion CH_2BrI^+ at different probe pulse polarizations.

molecular structure calculations of Dr. Tamás Rozgonyi. The details of those calculations are described more fully in Appendix A. Figure 4.22 shows the resulting potential energy surfaces for CH_2BrI as a function of the bending normal coordinate u_B. We choose to focus on this coordinate because the calculations indicate that the H atoms follow the carbon, as described at the beginning of this chapter, making CH_2BrI an essentially triatomic system. Moreover, the equilibrium bond lengths for the C-Br and C-I bonds change by $< 1\%$ in going from V_0^{neu} to V_0^{ion}. Therefore, the large potential energy changes along u_B make it the main coordinate of interest. We see a large displacement in bend angle of the equilibrium position for the ground neutral state V_0^{neu} and the ground ionic state V_0^{ion}, corresponding to an equilibrium I-C-Br angle of 95° in V_0^{neu} and 115° in V_0^{ion}. Several excited ionic states exist within a single photon (1.58 eV) energy separation from the ground ionic state. We will explore these states further in Section 4.3.

Although Fig. 4.22 shows the potential energy surfaces as a function of only one reaction coordinate, the PESs are known as a function of several reaction coordinates and can be so plotted. Figure 4.23 shows the calculated PESs for the ground ionic state V_0^{ion} of CH_2I_2, as a function of two geometric coordinates. The coordinates r (I-I separation) and R (the normal coordinate connecting r and the C atom) are shown in the accompanying diagram. The

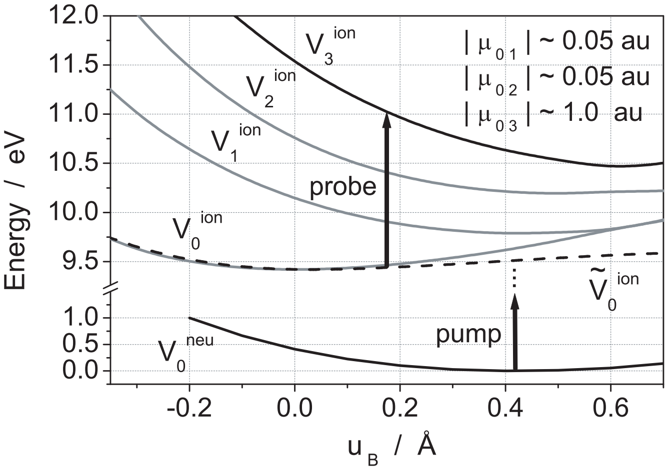

Figure 4.22: Calculated potential energy surfaces for CH_2BrI as a function of the bending normal coordinate u_B. The shading of the curves is roughly proportional to the strength of the transition dipole moment from V_0^{ion}. The dotted line indicates $\tilde{V}_0^{ion}$, the V_0^{ion} potential modified to emulate the effects of spin-orbit coupling. The values of the transition dipole moments for transitions from V_0^{ion} are also given in atomic units (au).

red star on the PES indicates the location of the equilibrium position in V_0^{neu}, the ground neutral state. Because the equilibria of the states are not the same, by promoting wavefunction to V_0^{ion}, we have created wavefunction at a non-equilibrium position. This implies that the wave function will evolve (move) with time, which is the definition of a wave packet.

Once the potentials for CH_2I_2 had been calculated, I was able to apply the split-operator method, as described by Tannor [84], to propagate a wave packet on the 2-dimensional ionic potential V_0^{ion}. The Matlab code to propagate two-dimensional wave packets is given in Appendix B. Frames from the resulting wave packet movie are shown in Figure 4.24. The initial wavefunction is the V_0^{neu} eigenfunction. The wave packet is launched on V_0^{ion} from the equilibrium position of V_0^{neu} and allowed to propagate in time.

Most of the resulting wave packet motion is along the diagonal coordinate from large r, small R values to small r, large R values. This diagonal coordinate corresponds roughly to the I-C-I bend angle. The motion is smooth and the wave packet remains compact through several oscillations. This can be seen in Figure 4.25, which shows the expectation values $\langle r \rangle$ and $\langle R \rangle$ as a function of time, as well as the overlap function between the initial wave packet and

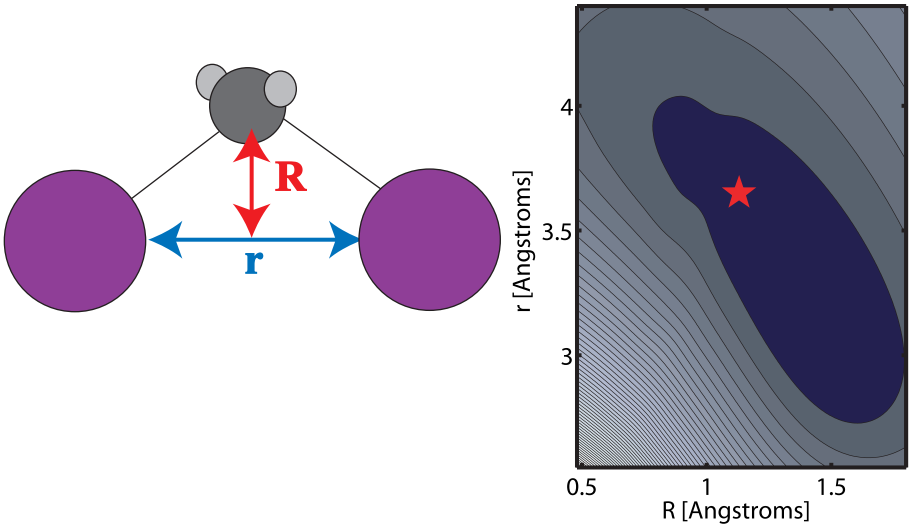

Figure 4.23: Calculated potential energy surface (at right) for V_0^{ion} in CH_2I_2 as a function of two geometric coordinates, r (the I-I separation) and R (the normal coordinate connecting r and the C atom, as shown at left). The red star indicates the location of the minimum in V_0^{neu}, the neutral ground state.

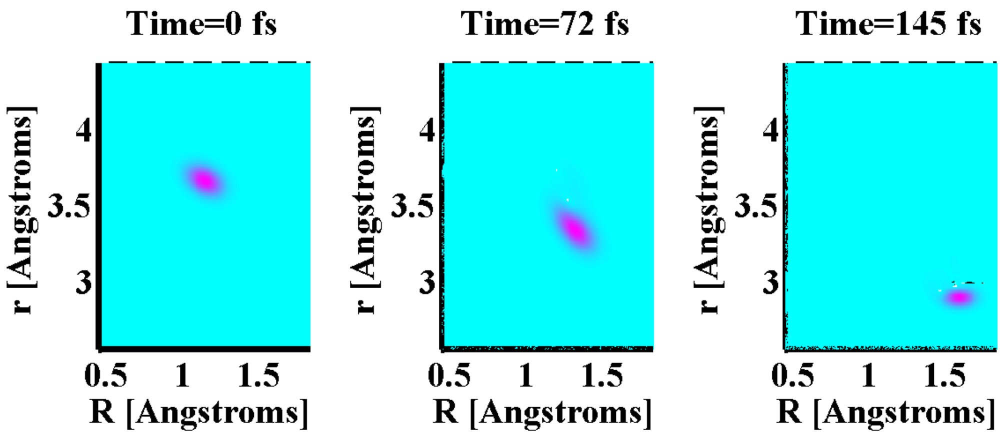

Figure 4.24: Frames from the movie of a wave packet propagating on the CH_2I_2 V_0^{ion} surface.

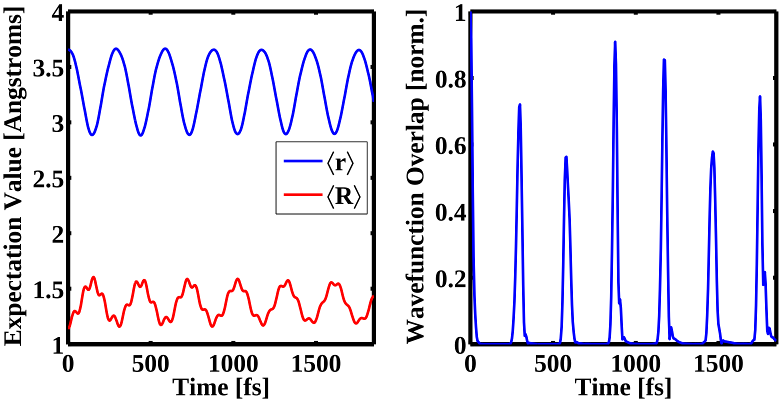

Figure 4.25: CH_2I_2 wave packet propagation results. Left: Expectation values ⟨r⟩ and ⟨R⟩ as a function of time, for r and R as shown in Fig. 4.23. Right: The overlap function for the wave packet vs. time, normalized to the wave function magnitude at 0 fs.

the evolving one, calculated as

$$\text{overlap} = \frac{\iint \psi^*(t)\psi(t=0)\,\mathrm{d}r\,\mathrm{d}R}{\iint \psi^*(t=0)\psi(t=0)\,\mathrm{d}r\,\mathrm{d}R},$$

where $\psi(t)$ is the wave function at time t.

We see that although the overlap function has sharp periodic spikes, it never returns to a value of 1. This is because of the small oscillations along the direction perpendicular to the long axis of the well, seen as fast oscillations in the value of ⟨R⟩. These fast oscillations are not always in phase with the larger oscillations, and this prevents the wave packet from returning to its exact starting location. At 740 fs and 1030 fs, where the fast oscillations are closest to being in phase with the main oscillations, we also have the largest values of the overlap function. The quantitative agreement between the calculations and the experimental data is excellent: the calculated potentials give an oscillation period of 290 fs, while the experimental oscillations at 114 cm^{-1} have a period of 292 fs. In combination with the experimental data described above, this strongly implies that the oscillations in $CH_2I_2^+$ and CH_2I^+ yields are a result of a resonant transfer from the wave packet oscillating in the V_0^{ion} potential.

4.3 Implications

The broad outline of the halomethane dynamics for all of the species discussed above can be given with a simple 3-state picture. Fig. 4.16, above, showed a cartoon of the essential states involved in the molecular dynamics. From the PES calculations, we now know that for CH_2BrI, the lowermost state is the ground neutral state V_0^{neu} and the middle state is the bound state $\tilde{V}_0^{ion}$, the ground ionic state. The uppermost state is an excited ionic state leading to dissociation, in this case V_3^{ion} [3]. The differences in the molecular ion yields can be explained by examining the details of their PESs. We first examine the case of CH_2BrI.

Fig. 4.22 shows a resonance with a strong transition dipole moment (TDM) between $\tilde{V}_0^{ion}$ and V_3^{ion} at $u_B \sim 0.18$ Å in the I-C-Br bending mode (I-C-Br angle $\sim 104°$). The resonance location being near (but not at) the center of $\tilde{V}_0^{ion}$ leads naturally to the presence of both the 94 cm^{-1} and 196 cm^{-1} modulations as the wave packet can be promoted to the final state twice per oscillation period if a probe pulse is incident on the molecule. Calculations of the population transfer versus pump-probe delay yield modulations containing both frequencies. Once the wave packet is promoted to V_3^{ion} of the asymmetric molecules, it is energetically possible to dissociate and bond-order analysis by Dr. Rozgonyi similar to [85, 86] indicates that C-I scission is likely from this state, consistent with previous dissociative photoionization experiments [87].

In the limit of weak coupling between $\tilde{V}_0^{ion}$ and V_3^{ion} by the probe pulse (low laser intensities), calculations indicate that the amount of wave packet transferred is independent of the wave packet momentum, as the wave packet (as seen in Figure 4.26) has almost exactly the same probability distribution (magnitude) at the resonance location moving to smaller angles (to the left) as moving to larger ones (to the right). This also agrees with the probe pulse energy scans seen in Fig. 4.17c, where the oscillations are symmetric at low probe pulse energies. Given that the magnitude of the wave packets is nearly identical, the only difference between left- and right- moving wave packets is the phase involved. However, both measurements and calculations indicate that for strong couplings, an asymmetry in the population transfer for the two different wave packet momenta appears, as discussed earlier (see Fig. 4.17c). For high intensities, the molecule can become completely transparent to the probe pulse for a left going wave packet, leading to negligible dissociation!

The calculations of this asymmetric transfer are shown in Figure 4.27a, which plots the calculated population transferred to V_3^{ion} from $\tilde{V}_0^{ion}$ as a func-

---

[3] Higher-lying states (V_4^{ion} and higher) are ignored because they are more than 1.58 eV from V_3^{ion} over the coordinate range under investigation.

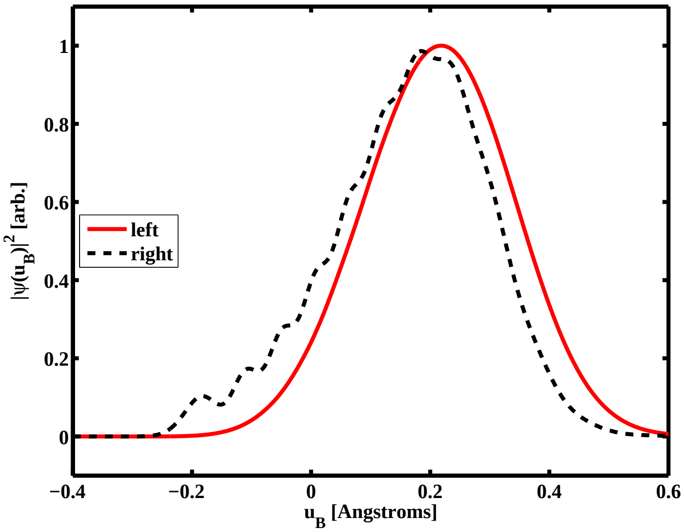

Figure 4.26: The calculated probability density for wave packets in $\tilde{\mathrm{V}}_0^{\mathrm{ion}}$ of $\mathrm{CH_2BrI^+}$ at 80 fs (left-moving) and 250 fs (right-moving) after the pump pulse. These times are the points when the wave packet is at the $\mathrm{FC_{probe}}$location.

tion of probe pulse field strength for two delay times that correspond to a left- and right-going wave packet at the resonance location $\mathrm{FC_{probe}}$. Our experimental measurements of the population transfer to $\mathrm{V_3^{ion}}$ as a function of probe pulse field strength are shown in Fig. 4.27b, which plots the depletion in the parent ion signal (depth of modulation in the oscillations) for delay times corresponding to left- and right-going wave packets at the resonance location. These measurements indicate that the dissociation for left- and right-going wave packets is roughly symmetric for weak coupling between the potentials (weak probe pulse field) but different for strong coupling (strong probe pulse field). Intensity volume averaging in the experiment keeps the population transfer for a left-going wave packet from returning to zero for high probe pulse energies. Because our laser has a Gaussian focus, higher intensities in the center of the focus, where left-going wave packets cannot be transferred, are balanced by the newly accessible volume on the edge of the focus, where intensities increasing from 0 allow left-going wave packets to be transferred. Dr. Rozgonyi's population transfer calculations including the intensity volume averaging (using a weighted average of calculations performed at different probe intensities) yield excellent agreement with our measurements, with a calculated right/left ratio of population transfer for strong probe fields of

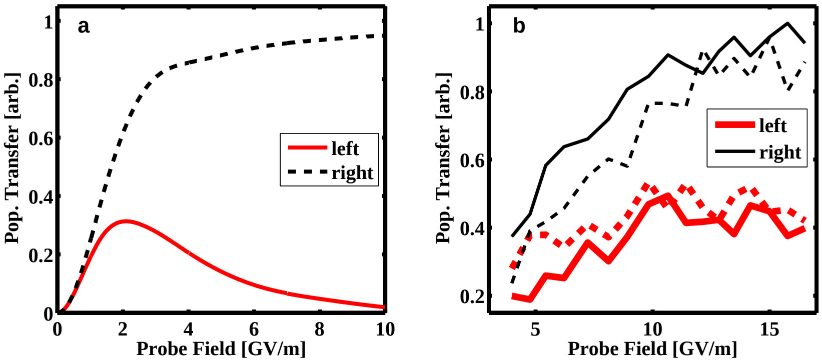

Figure 4.27: a) The calculated population transferred from $\tilde{\mathrm{V}}_0^{\mathrm{ion}}$ to $\mathrm{V}_3^{\mathrm{ion}}$ in $\mathrm{CH_2BrI}$ as a function of peak field strength for probe pulses at 2 delays: 80 fs (red solid) and 250 fs (black dashed), corresponding to the first (left-going) and second (right-going) times that the wave packet moves through $\mathrm{FC}_{\mathrm{probe}}$. b) The experimental population transfer, measured as a depletion from the parent (depth of modulation in the oscillations). The thick red solid and dashed lines represent population transferred for two different left-going wave packets. The thin black lines represent population transferred for two different right-going wave packets.

2.3 (experimental value $\sim$2.3)[4].

We already know the transfer involves a single-photon resonance, and both calculations and measurements indicate that the asymmetrical transfer is a strong-field effect. To understand the reasons behind this left/right transfer asymmetry, we turn to the dressed-state picture obtained by rediagonalizing the Hamiltonian to account for the states of the molecule in the presence of the light field. If we consider the potential energy surfaces in one dimension, it is relatively simple to calculate the adiabatic curves. Raise the lower state by γ, the energy of 1 photon (or lower the upper state by γ) to give the crossed diabatic states. Then for each position along the x axis, diagonalize the 2×2 Hamiltonian given by $\begin{bmatrix} V_3^{\mathrm{ion}}(x) - \gamma & \frac{\mu E}{\hbar} \\ \frac{\mu E}{\hbar} & V_0^{\mathrm{ion}}(x) \end{bmatrix}$. The new eigenvalues are the adiabatic potentials. Figure 4.28 shows the dressed-state picture for the ground and excited states of $\mathrm{CH_2I_2^+}$ at two different values of the field in the one-

---

[4] The volume averaging calculations included not only the spatial beam profile but also averaged over a uniform distribution of molecular orientations with respect to the probe pulse polarization. The value of 2.3 represents the ratio of population transfer for 80 fs and 250 fs after the pump pulse (left- and right-going wave packets).

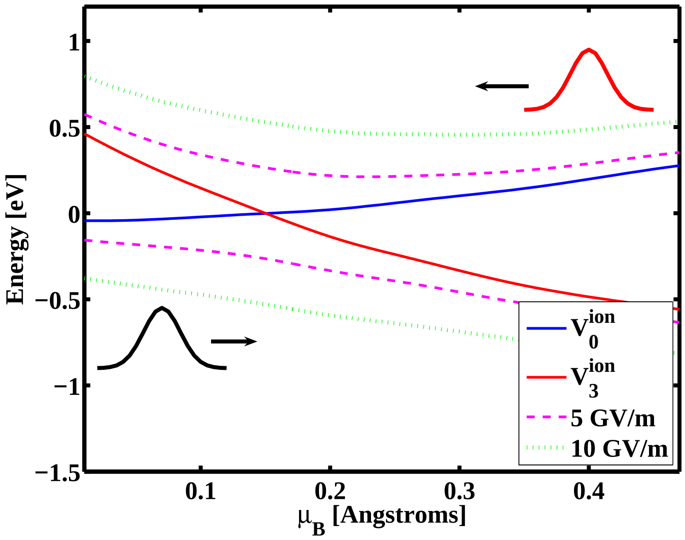

Figure 4.28: Dressed-state calculations for $CH_2I_2^+$ states $V_0^{\rm ion}$ and $V_3^{\rm ion}$. The dashed and dotted lines show the adiabatic curves for fields of 5 GV/m and 10 GV/m, respectively. Schematic wave packets are shown.

dimensional case, where u_B is the bending normal coordinate corresponding mostly to I-C-I bending angle. Thus, the potentials are roughly a linear cut along the long axis of the well seen in Fig. 4.23.

Figure 4.29 shows a similar calculation for the $\tilde{V}_0^{\rm ion}$ and $V_3^{\rm ion}$ potentials of CH_2BrI. Again, we see the dressed states near the resonance between $\tilde{V}_0^{\rm ion}$ and $V_3^{\rm ion}$ when coupled by the resonant probe pulse ($V_3^{\rm ion}$ shifted downwards by $h\nu$=1.58 eV). Now consider the wave packet motion on these dressed states. At low probe pulse field strengths, the adiabatic curves (purple dashed curves) lie close together, and the probability for the wave packet to jump between adiabatic states (i.e. non-adiabatic passage) is significant as the wave packet traverses the avoided crossing in either direction. Thus, right-going wave packets (black schematics) can be transferred by following the adiabatic curves, while left-going wave packets (red schematics) can be transferred via a combination of adiabatic and non-adiabatic passage. For instance, the left going wave packet might move left, jump the crossing in non-adiabatic passage, and turn around while the probe pulse is on. If it stays on the adiabatic curve on the return trip, it will end up on $V_3^{\rm ion}$ on the lower right hand side of Fig. 4.29. Other paths combining adiabatic and non-adiabatic passage are also possible. As long as the adiabatic curves are close together, some portion of the left-going wave packet will make it through the crossing to end up on $V_3^{\rm ion}$.

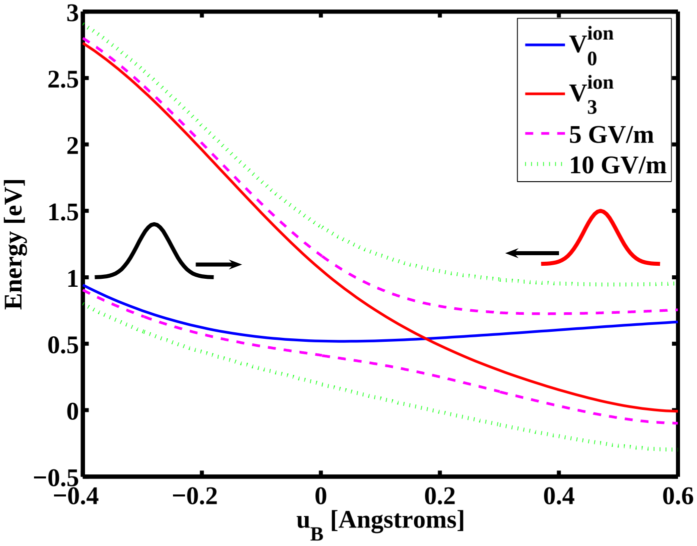

Figure 4.29: Dressed-state calculations for CH_2BrI^+ states $\tilde{V}_0^{ion}$ and V_3^{ion}. The dashed and dotted lines show the adiabatic curves for fields of 5 GV/m and 10 GV/m, respectively. Schematic wave packets are shown.

In the case of a strong probe pulse field, the dressed states (green dotted curves) are well separated and the wave packet adiabatically follows them (the probability of non-adiabatic passage is very small). The left-going wave packet enters on the upper adiabatic state, and turns around before passing through the avoided crossing. It therefore stays on $\tilde{V}_0^{ion}$ and does not dissociate. The right-going wave packet enters on the lower adiabatic potential and does not return to the avoided crossing while the probe pulse is on. As the character of the dressed states changes in passing through the avoided crossing, the right-going wave packet finds itself on V_3^{ion} after passing through the avoided crossing once on the lower adiabatic state.

Although our results are somewhat similar to [19] and [20], where left- and right-going wave packets also displayed asymmetric transfer, those results relied on the wave function having different shapes when moving left and right. As shown in Fig. 4.26, the probability distributions are nearly identical for left- and right-going wave packets on the $\tilde{V}_0^{ion}$ potential of CH_2BrI. The combination of the wave packet momentum and shape of the dressed states leads to the asymmetry in dissociation yields for strong probe fields. The dynamics here are similar to those responsible for 'molecular bond locking', as discussed in [88]. In the bond locking case, the application of a strong field resonant with a dressed state transition keeps a bond length locked at a non-equilibrium length. The diabatic states have a steep slope in the vicinity of the crossing, and so as long as the field is on, the wave packet is trapped on the upper adiabatic state and undergoes small oscillations about the crossing position, which corresponds to a non-equilibrium length. However, because $\tilde{\mathrm{V}}_0^{\mathrm{ion}}$ is not as steep as $\mathrm{V}_3^{\mathrm{ion}}$ in the vicinity of the resonance, in our case the wave packet is not locked in position, but rather trapped on $\tilde{\mathrm{V}}_0^{\mathrm{ion}}$ when it is moving left and completely transferred between $\tilde{\mathrm{V}}_0^{\mathrm{ion}}$ and $\mathrm{V}_3^{\mathrm{ion}}$ when moving right.

As discussed earlier, $\mathrm{CH_2ClI}$ has very similar dynamics to $\mathrm{CH_2BrI}$, and we expect that the same explanation should hold. By contrast, $\mathrm{CH_2Br_2}$ and $\mathrm{CH_2I_2}$ have only a single frequency of ion yield oscillation for most energies[5]. Several possible explanations for the missing second frequency in the symmetric molecules exist.

1. Symmetric molecules have a much stronger left-right transfer asymmetry, such that left-going wave packets have essentially no transfer to the dissociative state.

2. The excited ionic states in these molecules are shaped in such a way that a wave packet which arrives on them with left-going momentum is returned through a crossing to the ground ionic state (or another bound ionic state), whereas wave packets with right-going momentum can ride over any barrier to dissociation.

3. The resonance in the symmetric molecules is so close to the turning point on the ground ionic potential that there is only one opportunity per cycle to resonantly transfer the wave packet to an excited potential. If the resonance can only be reached once per cycle, we would expect to see only the fundamental oscillation, and not any second harmonic.

Very recent work by Dr. Rozgonyi has helped to distinguish among these possibilities. He calculates a TDM for the $\mathrm{V}_0^{\mathrm{ion}}$ to $\mathrm{V}_3^{\mathrm{ion}}$ transition in $\mathrm{CH_2I_2^+}$ of 1.8 au, nearly twice the value of 1.0 au for the corresponding transition in $\mathrm{CH_2BrI^+}$. This implies that for a given field strength, there will be a larger asymmetry in the transfer for left- and right-going wave packets, or equivalently, that $\mathrm{CH_2I_2^+}$ signals will tend to go to a single frequency at roughly half the field strength that $\mathrm{CH_2BrI^+}$ signals do. This may help explain some of the qualitative differences between Fig. 4.17b and c.

However, an even more important factor in our ability to experimentally resolve the second harmonic may be the location of $\mathrm{FC_{probe}}$. Preliminary analysis in $\mathrm{CH_2I_2}$ shows that $\mathrm{FC_{probe}}$ is very close to the outer turning point

---

[5] The fast oscillations in $\langle R \rangle$ from Fig. 4.25 would be near the limits of our temporal resolution, even if they had an impact on the ionic fragment yields.

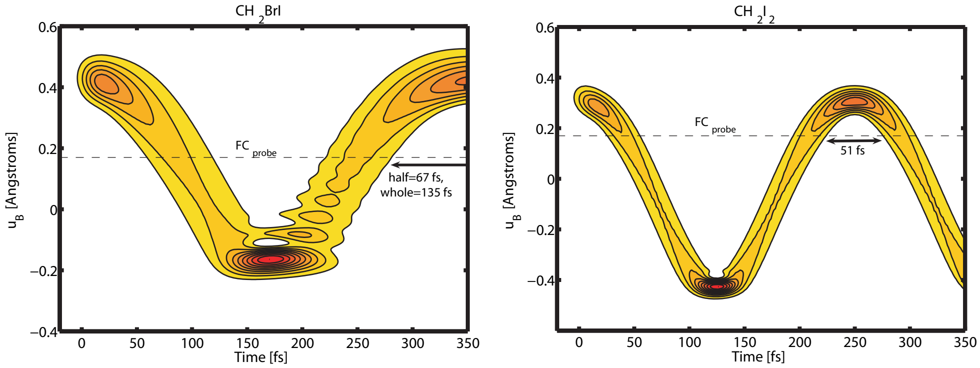

Figure 4.30: A contour plot of the wave packet location as a function of time for CH_2BrI (left) and CH_2I_2 (right). Note the amount of time that the wave packet is not in the FC-probe region. Plots are based on preliminary calculations by Dr. Rozgonyi.

of the V_0^{ion} potential. When the dynamics are modeled with a realistic wave packet, there is a gap of only 50 fs when the wave packet is at the outer turning point and not in the FC_{probe} region. By contrast, in CH_2BrI, the equivalent gap is $\sim$150 fs, as can be seen in Figure 4.30. As our pulses are $\sim$30–35 fs long, we easily have the temporal resolution to see the latter situation in our experimental data, but we are approaching the limits of our system in the former. As the oscillations in CH_2Br_2 are even faster (round trip time of 197 fs vs. 292 fs in CH_2I_2), if it has a similar set of PESs to CH_2I_2, it is not surprising that we only see the fundamental oscillations. The only ways around these experimental limitations would be to use a shorter probe pulse or to somehow narrow the shape of the wavepacket created on $V_0^{ion}/\tilde{V}_0^{ion}$. Although these observations are based on tentative calculations of the wave packet widths near FC_{probe}, this may help explain some of the contrast between the symmetric and asymmetric molecules. Ongoing investigations seek to further clarify this explanation.

The experimental data not only tell us about the potential energy surfaces of the molecules; they also indirectly reveals some aspects of the orbital structure, as the orbital structure and PESs are connected. We see from the energy scans (Figs. 4.12-4.15) that when a weak pulse starts ionizing, it does not create solely parent ion. Rather, several large ions appear at about the same energy. This indicates that the initial pump pulse is not creating a wave packet purely on $V_0^{ion}/\tilde{V}_0^{ion}$. Instead, the pump pulse is exciting small amounts of wave packet on several states, some of which are dissociative. This is consistent with the picture of tunnel ionization given in [89]; if the effective ionization potentials of two states are similar, both are likely to be accessed by tunnel ionization. It is only if the ionization potentials of the lowest ionic state (HOMO) and the higher lying ionic states are very different that ionization will be strictly from the HOMO. Given the relative energies in our calculated PESs for CH_2I_2 and CH_2BrI, V_1^{ion} is likely to be populated. From the molecular structure calculations, we know that in CH_2BrI, $\tilde{V}_0^{ion}$ and V_1^{ion} are coupled by an avoided crossing (when spin-orbit effects are included). Because the surfaces are multidimensional, any wave function on V_1^{ion} may leak through to $\tilde{V}_0^{ion}$, but it is not likely to return to the crossing in such a way as to go back onto V_1^{ion}. Therefore, a slow one-way transfer from V_1^{ion} into $\tilde{V}_0^{ion}$ is likely. This one-time decay after the initial pump pulse is likely to be responsible for the overall dynamics seen in the pump probe scans (Fig. 4.6), where the parent ion yield slowly drops after time zero and never recovers, while the major daughter ion yields (CH_2Br^+ and CH_2I^+) increase. The probe pulse is only resonant to dissociative states from $\tilde{V}_0^{ion}$, and so it has to wait for all of the wave function to leak into $\tilde{V}_0^{ion}$ from V_1^{ion}.

As for how all of this relates to the orbital structure, we know that ionizing to the V_0^{ion} state of a molecule corresponds roughly to ionizing from the HOMO. Ionizing to the V_1^{ion} state corresponds to ionizing from the HOMO-1 (the second highest occupied molecular orbital). In general, these two orbitals will have different structure and thus different polarizabilities. We can probe the orbital structure by varying the relative polarizations of our pump and probe pulses, as seen in Figs. 4.19-4.21, because the tunnel ionization is sensitive to the shape of the orbital and the angle of the ionizing laser polarization relative to the axes of the orbital. As discussed above, although the overall decay from before to after time zero does not change appreciably when the probe pulse polarization is rotated (with fixed pump polarization), the amplitude of the oscillations does change. The oscillations have a substantially larger amplitude (at least 15% larger) for perpendicular polarizations than for parallel ones. This implies that V_1^{ion} is comparatively insensitive to the polarizations, while V_0^{ion} is sensitive to the relative polarizations. The latter is expected, as the transition from V_0^{ion} to the dissociative states such as V_3^{ion} in CH_2BrI and CH_2I_2 is single-photon, and for single-photon resonant transitions, the dipole moment is important.

Our work in the halomethane family has highlighted the importance of single-photon dynamic resonances in dissociation reactions. We have shown that in many respects, molecular structure calculations yield excellent quantitative agreement with experimental results, and we have demonstrated that a three-level system of potential energy surfaces explains much of the dynamics within several members of the halomethane family. The molecular dynamics on a dressed-state picture revealed that wave packet phase can play an important role in the efficiency of transfer. Polarization experiments hint at further details of the alignment and molecular orbital characteristics which may be revealed with additional work in the near future.

Chapter 5

Conclusion

This thesis has explored the nature of dissociation dynamics in small molecules, including several members of a molecular family. We started with the construction of a molecular beam chamber that could facilitate molecular alignment experiments. We continued with alignment experiments in nitrogen, which showed how ionization and dissociation are affected by the molecular orbital structure. Using our strong-field laser pulses, we could affect the multiple ionization of nitrogen to N_2^{++} and the dissociative daughter ions $N^+(1,0)$ and $N^+(1,1)$. We also found that rescattering was the main source of double ionization in N_2, as elliptical polarizations greatly decrease the yield of the fragments produced in double ionization. The relative angle of pump and probe linear polarizations also affected yields, as was expected based on the asymmetric molecular orbital structure.

Many of the same mechanisms are involved in the ionization and dissociation of the larger halomethane molecules. Again, the molecules are ionized by a strong-field tunnel ionization, and subsequent probe pulses can control the dissociation. We found that for several of the CH_2XY molecules, a 3-level potential energy structure (Fig. 4.16) was sufficient to explain much of the variation in ion yields with time delay and probe intensity. The wave packet is initially promoted from the ground state to the middle state by tunnel ionization. In general, a large displacement in X-C-Y bending angle between the equilibrium positions of the ground neutral and ground ionic states means that the wave packet oscillates in the ground ionic state. At some position (the FC_{probe} location), the wave packet passes through a single-photon resonance to a higher-lying ionic state, from which it can ride over any barriers to dissociation. The location of FC_{probe} relative to the turning points of the well determines the details of the resulting ionic yield oscillations, which occur as the parent ion is promoted to the dissociative state.

This three-level picture, based on molecular structure calculations, is in close quantitative and qualitative agreement with our experimental results. We have demonstrated that in CH_2BrI, resonant transfer is dependent not on the amplitude of the molecular wave packet (as in previous control experiments), but on the phase. This momentum-dependent transfer relies on strong-field steering by the laser on a light-dressed potential energy surface.

However, the one-dimensional three-level model is insufficient to fully explain all details of the halomethane experimental ion yields. For that we must take into consideration additional levels and dimensions, identical to considering a more complicated molecular orbital structure. For instance, the dissociation from V_3^{ion} can only be modeled with at least one additional dissociation coordinate. A further complication arises because the initial ionization does not create a pure V_0^{ion} population, or equivalently, it does not ionize strictly from the HOMO state. Rather, a combination of HOMO and lower-lying orbitals are ionized, meaning population is created in both V_0^{ion} and V_1^{ion}. The orbitals have different structure, leading to differences in their response to changing polarizations. The V_1^{ion} population leaks slowly into V_0^{ion}, yielding a slow decay in the parent ion yield as the wave packet becomes accessible to the resonant probe pulse. This slow leak also means that chirped pulses can access more of the wave packet and transfer a greater portion of the ionic population to the dissociative state. The combination of orbitals involved also hints at alignment dependence, although we did not directly align rotationally cold molecular samples. In particular, the decay of enhanced oscillations for perpendicular probe polarizations suggests a rotational factor comes into play.

Future experiments aim to refine these alignment details. A two-stage extraction system planned for the molecular beam chamber will give enhanced resolution in the time-of-flight system. Meanwhile, calculations currently underway will help finalize the involvement of various orbitals and potential energy surfaces in the halomethanes. Additional quantitative comparisons in CH_2Br_2 and CH_2ClI will help refine the details gained from our understanding of the dynamics in CH_2I_2 and CH_2BrI. This will continue to enhance our systematic understanding of the dynamics of ionization and dissociation in small molecules.

Bibliography

[1] A. H. Zewail, *Femtochemistry – Ultrafast Dynamics of The Chemical Bond, Vol. I and II* (World Scientific, Singapore, 1994).

[2] R. N. Zare, Science **279**, 1875 (1998).

[3] T. Brixner and G. Gerber, Chem. Phys. Chem. **4**, 418 (2003).

[4] E. Skovsen, H. Stapelfeldt, S. Juhl, and K. Mølmer, Phys. Rev. Lett. **91**, 090406 (2003).

[5] S. Gräfe, D. Scheidel, V. Engel, N. E. Henriksen, and K. B. Møller, J. Phys. Chem. A **108**, 8954 (2004).

[6] J. Itatani, J. Levesque, D. Zeidler, H. Niikura, H. Pépin, J. C. Kieffer, P. B. Corkum, and D. M. Villeneuve, Nature **432**, 867 (2004).

[7] I. Ben-Itzhak, P. Q. Wang, J. F. Xia, A. M. Sayler, M. A. Smith, K. D. Carnes, and B. D. Esry, Phys. Rev. Lett. **95**, 073002 (2005).

[8] K. Ohmori, H. Katsuki, H. Chiba, M. Honda, Y. Hagihara, K. Fujiwara, Y. Sato, and K. Ueda, Phys. Rev. Lett. **96**, 093002 (2006).

[9] T. Seideman, M. Y. Ivanov, and P. B. Corkum, Phys. Rev. Lett. **75**, 2819 (1995).

[10] M. J. DeWitt and R. J. Levis, J. Chem. Phys. **108**, 7045 (1998).

[11] R. J. Levis and M. J. DeWitt, J. Phys. Chem. A **103**, 6493 (1999).

[12] W. Fuß, W. E. Schmid, and S. A. Trushin, J. Chem. Phys. **112**, 8347 (2000).

[13] M. Lezius, V. Blanchet, D. M. Rayner, D. M. Villeneuve, A. Stolow, and M. Y. Ivanov, Phys. Rev. Lett. **86**, 51 (2001).

[14] M. Lezius, V. Blanchet, M. Y. Ivanov, and A. Stolow, J. Chem. Phys. **117**, 1575 (2002).

[15] S. A. Trushin, W. Fuß, and W. E. Schmid, J. Phys. B **37**, 3987 (2004).

[16] S. Smith, A. Markevitch, D. Romanov, X. Li, R. Levis, and H. Schlegel, J. Phys. Chem. A **108**, 11063 (2004).

[17] L. V. Keldysh, Sov. Phys. JETP **20**, 1307 (1965).

[18] D. Cardoza, B. J. Pearson, and T. Weinacht, J. Chem. Phys. **126**, 084308 (2007).

[19] P. Cong, G. Roberts, J. L. Herek, A. Mohktari, and A. H. Zewail, J. Phys. Chem. **100**, 7835 (1996).

[20] B. Kohler, V. V. Yakovlev, J. Che, J. L. Krause, M. Messina, K. R. Wilson, N. Schwentner, R. M. Whitnell, and Y. Yan, Phys. Rev. Lett. **74**, 3360 (1995).

[21] H. Harada, S. Shimizu, T. Yatsuhashi, S. Sakabe, Y. Izawa, and N. Nakashima, Chem. Phys. Lett. **342**, 563 (2001).

[22] L. Robson, K. W. D. Ledingham, A. D. Tasker, P. McKenna, T. McCanny, C. Kosmidis, D. A. Jaroszynski, D. R. Jones, R. C. Issac, and S. Jamieson, Chem. Phys. Lett. **360**, 382 (2002).

[23] H. Harada, M. Tanaka, M. Murakami, S. Shimizu, T. Yatsuhashi, N. Nakashima, S. Sakabe, Y. Izawa, S. Tojo, and T. Majima, J. Phys. Chem. A **107**, 6580 (2003).

[24] B. J. Pearson, S. R. Nichols, and T. C. Weinacht, J. Chem. Phys. **127**, 131101 (2007).

[25] S. R. Nichols, T. Rozgonyi, B. J. Pearson, and T. C. Weinacht (2008), submitted.

[26] S. R. Nichols, D. Geissler, T. Rozgonyi, B. J. Pearson, and T. Weinacht (2008), in prep.

[27] M. A. Dugan, J. X. Tull, and W. S. Warren, J. Opt. Soc. Amer. B **14**, 2348 (1997).

[28] F. Langhojer, D. Cardoza, M. Baertschy, and T. Weinacht, J. Chem. Phys. **122**, 014102 (2005).

[29] A. M. Weiner, **19**, 161 (1995).

[30] B. J. Pearson, J. L. White, T. C. Weinacht, and P. H. Bucksbaum, Phys. Rev. A **63**, 063412 (2001).

[31] T. C. Weinacht and P. H. Bucksbaum, **4**, R35 (2002).

[32] D. Zeidler, S. Frey, K.-L. Kompa, D. Proch, and M. Motzkus, Phys. Rev. A **64**, 023420 (2001).

[33] D. M. Cardoza, Ph.D. thesis, Stony Brook University, Stony Brook, NY (2006).

[34] R. Trebino, K. W. DeLong, D. N. Fittinghoff, J. N. Sweetser, M. A. Krumbugel, B. A. Richman, and D. J. Kane, Rev. Sci. Inst. **68**, 3277 (1997).

[35] P. Nürnberger, Master's thesis, Stony Brook University, Stony Brook, NY (2003).

[36] S. Akturk, M. Kimmel, P. O'Shea, and R. Trebino, Optics Express **11**, 491 (2003).

[37] P. O'Shea, M. Kimmel, X. Gu, and R. Trebino, Opt. Lett. **26**, 932 (2001).

[38] *Labview 7.0* (National Instruments, 2003).

[39] D. R. Miller, *Atomic and Molecular Beam Methods Vol. 1* (Oxford University Press, USA, 1988), chap. 2, Free Jet Sources, pp. 14–53.

[40] P. Linstrom and W. Mallard, eds., *NIST Chemistry WebBook, NIST Standard Reference Database Number 69* (National Institute of Standards and Technology, Gaithersburg, MD, 20899, 2008), http://webbook.nist.gov, (retrieved Nov. 1, 2008).

[41] T. Seideman, Phys. Rev. Lett. **83**, 4971 (1999).

[42] T. Seideman, J. Chem. Phys. **103**, 7887 (1995).

[43] H. Stapelfeldt and T. Seideman, Rev. Mod. Phys. **75**, 543 (2003).

[44] D. Cardoza, F. Langhojer, C. Trallero-Herrero, O. L. A. Monti, and T. Weinacht, Phys. Rev. A **70**, 053406 (2004).

[45] D. Cardoza, M. Baertschy, and T. Weinacht, Chem. Phys. Lett. **411**, 311 (2005).

[46] Z. X. Zhao, X. M. Tong, and C. D. Lin, Phys. Rev. A **67**, 043404 (2003).

[47] T. Kanai, S. Minemoto, and H. Sakai, Nature **435**, 470 (2005).

[48] J. McKenna, M. Suresh, B. Srigengan, I. D. Williams, W. A. Bryan, E. M. L. English, S. L. Stebbings, W. R. Newell, I. C. E. Turcu, J. M. Smith, et al., Phys. Rev. A **73**, 043401 (2006).

[49] V. Loriot, E. Hertz, A. Rouzée, B. Sinardet, B. Lavorel, and O. Faucher, Opt. Lett. **31**, 2897 (2006).

[50] D. Pavičić, K. F. Lee, D. M. Rayner, P. B. Corkum, and D. M. Villeneuve, Phys. Rev. Lett. **98**, 243001 (2007).

[51] R. Coffee and G. Gibson, Phys. Rev. A **72**, 011401 (2005).

[52] A. S. Alnaser, S. Voss, X.-M. Tong, C. M. Maharjan, P. Ranitovic, B. Ulrich, T. Osipov, B. Shan, Z. Chang, and C. L. Cocke, Phys. Rev. Lett. **93**, 113003 (2004).

[53] P. Corkum, N. Burnett, and F. Brunel, Phys. Rev. Lett. **62**, 1259 (1989).

[54] M. P. Hertlein and P. H. Bucksbaum, Ph.D. thesis, University of Michigan (2000).

[55] G. Gibson, R. Freeman, and T. McIlrath, Phys. Rev. Lett. **67**, 1230 (1991).

[56] R. R. Freeman, P. H. Bucksbaum, H. Milchberg, S. Darack, D. Schumacher, and M. E. Geusic, Phys. Rev. Lett. **59**, 1092 (1987).

[57] J. G. Story, D. I. Duncan, and T. F. Gallagher, Phys. Rev. A **50**, 1607 (1994).

[58] J. P. Nibarger, S. V. Menon, and G. N. Gibson, Phys. Rev. A **63**, 053406 (2001).

[59] X. Tong, Z. Zhao, A. Alnaser, S. Voss, C. Cocke, and C. Lin, J. Phys. B **38**, 333 (2005).

[60] M. Baertschy, *Trifluoroacetone rotation times* (2005), private communication.

[61] W. C. Wiley and I. H. McLaren, Rev. Sci. Inst. **26**, 1150 (1955).

[62] M. Kawasaki, S. J. Lee, and R. Bersohn, J. Chem. Phys. **62**, 809 (1975).

[63] L. J. Butler, E. J. Hintsa, S. F. Shane, and Y. T. Lee, J. Chem. Phys. **86**, 2051 (1987).

[64] S. J. Lee and R. Bersohn, J. Phys. Chem. **86**, 728 (1982).

[65] T. Takayanagi and A. Yokoyama, Bull. Chem. Soc. Jap. **68**, 2225 (1995).

[66] J. C. Williamson, J. Cao, H. Ihee, H. Frey, and A. H. Zewail, Nature **386**, 159 (1997).

[67] J. C. Mössinger, D. E. Shallcross, and R. A. Cox, Faraday Trans. **94**, 1391 (1998).

[68] I. Pastirk, E. J. Brown, Q. Zhang, and M. Dantus, J. Chem. Phys. **108**, 4375 (1998).

[69] X. Zheng and D. L. Phillips, J. Chem. Phys. **113**, 3194 (2000).

[70] D. Bingemann, A. M. King, and F. F. Crim, J. Chem. Phys. **113**, 5018 (2000).

[71] D. G. Abrashkevich, M. Shapiro, and P. Brumer, J. Chem. Phys. **116**, 5584 (2002).

[72] A. Tarnovsky, M. Wall, M. Gustafsson, N. Lascoux, V. Sundstrom, and E. Akesson, J. Phys. Chem. A **106**, 5999 (2002).

[73] D. Cardoza, C. Trallero-Herrero, F. Langhojer, H. Rabitz, and T. Weinacht, J. Chem. Phys. **122**, 124306 (2005).

[74] J. Davidsson, J. Poulsen, M. Cammarata, P. Georgiou, R. Wouts, G. Katona, F. Jacobson, A. Plech, M. Wulff, G. Nyman, et al., Phys. Rev. Lett. **94**, 245503 (2005).

[75] K. D. Goodwin, W. J. North, and M. E. Lidstrom, Limnology and Oceanography **42**, 1725 (1997).

[76] L. Carpenter, W. Sturges, S. Penkett, P. Liss, B. Alicke, K. Hebestreit, and U. Platt, J. Geophys. Res. **104**, 1679 (1999).

[77] N. J. Warwick, J. A. Pyle, G. D. Carver, X. Yang, N. H. Savage, F. M. OConnor, and R. A. Cox, J. Geophys. Res. **111**, D24305 (2006), doi:10.1029/2006JD007264.

[78] R. S. Judson and H. Rabitz, Phys. Rev. Lett. **68**, 1500 (1992).

[79] D. J. Tannor, R. Kosloff, and S. A. Rice, J. Chem. Phys. **85**, 5805 (1986).

[80] D. Geissler, B. J. Pearson, and T. C. Weinacht, J. Chem. Phys. **127**, 204305 (2007).

[81] M. Lee, H. Kim, Y. S. Lee, and M. S. Kim, J. Chem. Phys. **122**, 244319 (2005).

[82] M. Lee, H. Kim, Y. S. Lee, and M. S. Kim, J. Chem. Phys. **123**, 024310 (2005).

[83] M. V. Ammosov, N. B. Delone, and V. P. Krainov, Sov. Phys.–JETP **64**, 1191 (1986), zh. Eksp. Teor. Fiz. 91, 2008 (1986).

[84] D. Tannor, *Introduction to Quantum Mechanics: A Time-Dependent Perspective* (University Science Books, Herndon, VA, 2006).

[85] I. Mayer and A. Gömöry, Chem. Phys. Lett. **344**, 553 (2001).

[86] I. Mayer and A. Hamza, *Program "APOST", Version 1.09* (2004), http://occam.chemres.hu/programs.

[87] A. F. Lago, J. P. Kercher, A. Bödi, B. Sztáray, B. Miller, D. Wurzelmann, and T. Baer, J. Phys. Chem. A **109**, 1802 (2005).

[88] T. Szakács, B. Amstrup, P. Gross, R. Kosloff, H. Rabitz, and A. Lörincz, Phys. Rev. A **50**, 2540 (1994).

[89] X. M. Tong, Z. X. Zhao, and C. D. Lin, Phys. Rev. A **66**, 033402 (2002).

[90] M. J. Frisch, G. W. Trucks, H. B. Schlegel, G. E. Scuseria, M. A. Robb, J. R. Cheeseman, J. A. M. Jr, T. Vreven, K. N. Kudin, J. C. Burant, et al., *Gaussian 2003* (Gaussian Inc., 2003).

[91] M. Casida, *Recent Advances in Density Functional Methods, Part I* (World Scientific, Singapore, 1995), p. 155.

[92] P. J. Stephens, F. J. Devlin, C. F. Chabalowski, and M. J. Frisch, J. Phys. Chem. **98**, 11623 (1994).

[93] K. A. Peterson, D. Figgen, E. Goll, H. Stoll, and M. Dolg, J. Chem. Phys. **119**, 11113 (2003).

[94] M. Lee and M. S. Kim, Chem. Phys. Lett. **431**, 19 (2006).

[95] B. Roos and P. Taylor, J. Phys. Chem. **48**, 157 (1980).

[96] M. C. and G. Balint-Kurti, J. Chem. Phys. **91**, 3571 (1989).

[97] M. D. Feit, J. A. Fleck, and A. Steiger, J. Comput. Phys. **47**, 412 (1982).

[98] J. A. Fleck, J. R. Morris, and M. D. Feit, Appl. Phys. A **10**, 129 (1976).

[99] D. Kosloff and R. Kosloff, J. Comput. Phys. **52**, 35 (1982).

Appendix A

Molecular Structure Calculations

Calculations of the potential energy surfaces for CH_2BrI and CH_2I_2 were implemented according the following scheme by Dr. Tamás Rozgonyi. We provide the details for CH_2BrI, since that molecule was used for more extensive calculations, but similar methods were used for CH_2I_2. The author thanks Dr. Rozgonyi for providing the information contained herein.

The Gaussian03 package of programs [90] was used and both density functional theory and time-dependent density functional theory (TDDFT; [91]) with the B3LYP functional [92] were applied to calculate the equilibrium geometries[1], the normal mode coordinates[2], and the relevant potential energy curves for CH_2BrI. The aug-cc-pVTZ basis set was used for H, C and Br atoms, while for the I atom the aug-cc-pVTZ-PP basis set reported in [93] was used. The C_S symmetry constraint was also applied. The potentials computed by TDDFT could be well fitted in the important coordinate range by Morse potentials of the form $V_i^q = D_i^q(1 - \exp(-\beta_i^q(u - u_i^q)))^2 + C_i^q$. Setting $u_0^{ion} = 0$ and $C_0^{neu} = 0$, the rest of the parameters are: $D_0^{neu} = 7.0651$ eV, $\beta_0^{neu} = 5.1511$ nm^{-1}, $u_0^{neu} = 0.042$ nm, $D_0^{ion} = 4.169$ eV, $\beta_0^{ion} = 6.5317$ nm^{-1},

---

[1] The equilibrium geometry of the CH_2BrI^+cation is r(C-I)=2.1542 Å, r(C-Br)=1.9376 Å, and r(C-H)=1.0815 Å, with Br-C-I and I-C-H angles of 95.4811° and 110.4184°, respectively, and a dihedral angle of 115.0077°. The equilibrium geometry of the neutral CH_2BrI molecule in its ground electronic state is r(C-I)=2.1563 Å, r(C-Br)=1.9435 Å, r(C-H)=1.0802 Å, with Br-C-I and I-C-H angles of 114.8723° and 107.0424° and a dihedral angle of 119.646°.

[2] The normal coordinate displacements (dx, dy, dz) of the atoms C, Br and I for the "bending" vibration of the CH_2BrI^+ cation in its ground electronic state are (0.43, -0.08, 0), (0.01, -0.60, 0) and (-0.05, 0.38, 0) respectively. The reduced mass is 49.92 amu. The displacements of the hydrogen atoms are (0.39, -0.01, $\mp$0.02). The equilibrium coordinates (x, y, z) in Å for the C, Br, I and H atoms are (-1.19585, -0.54115, 0), (0.30567, -1.76579, 0), (0, 1.25063, 0) and (-1.76167, -0.61712, $\pm$0.91851) respectively.

$C_0^{ion} = 9.42$ eV, $D_3^{ion} = 10^3$ eV, $\beta_3^{ion} = 0.5$ nm^{-1}, $u_3^{ion} = 0.0631$ nm and $C_0^{ion} = 10.5145$ eV.

The ground-state electron configuration of the CH_2BrI^+ cation in its equilibrium geometry is $...(23a')^2(9a'')^2(10a'')^2(24a')^1(25a')^0$ when only the valence orbitals are considered. Considering the C-I bond as the X axis and the I-C-Br plane as the XY plane, the $10a''$ and $24a'$ mainly correspond to the nonbonding lone pair orbitals on iodine perpendicular (n_Z(I)) and parallel (n_Y(I)) to the molecular plane, respectively. $9a''$ mainly corresponds to the nonbonding lone pair orbital on bromine (n_Z(Br)) perpendicular to the molecular plane. The lowest three electronic excited states (V_1^{ion}, V_2^{ion}, and V_3^{ion}) of the cation at the ground-state equilibrium geometry can be described by one-electron excitations $n_Z(\mathrm{I}) \rightarrow n_Y(\mathrm{I})$ ($10a'' \rightarrow 24a'$), $n_Z(\mathrm{Br}) \rightarrow n_Y(\mathrm{I})$ ($9a'' \rightarrow 24a'$), and $n_X(\mathrm{I}) \rightarrow n_Y(\mathrm{I})$ ($23a' \rightarrow 24a'$).

As the displacement of the ground state of the ion relative to the neutral equilibrium geometry is mostly along the I-C-Br bending normal coordinate u_B, the potential energies for the first four ionic states were calculated as a function of this coordinate. Fig. 4.22 shows these states, along with the neutral ground state, as a function of u_B. The equilibrium I-C-Br angle for the CH_2BrI^+ cation is 95.5° (u_B=0 Å), while the equilibrium I-C-Br angle of the neutral CH_2BrI molecule in its ground electronic state is 114.9° (u_B=0.42 Å).

As discussed in the literature [81, 82, 94] there is a strong spin-orbit (SO) coupling between the ground and the first excited ionic states of CH_2XI molecules. For CH_2BrI^+ this results in a bending vibrational frequency much lower than the 137 cm^{-1} obtained without SO-coupling and produces a large anharmonicity (the measured vibrational frequencies for n=0, 7, and 8 are $\nu_0 = 116$ cm^{-1}, 98.1 cm^{-1}, and 95.7 cm^{-1}, respectively [81].) In order to be consistent with these measurements without explicitly including SO coupling in the TDDFT calculations, a half-harmonic term[3] was added to the V_0^{ion} (a^2A') potential to emulate the effect of the coupling to V_1^{ion} (a^2A'') on the shape of the ground ionic state. The resulting $\tilde{V}_0^{\mathrm{ion}}$ was used throughout the propagation. Although both TDDFT and preliminary complete active space self-consistent field computations [95] suggest that V_2^{ion} (b^2A'') and V_3^{ion} (b^2A') cross close to FC_{pump}, and thus SO-coupling between these two states should be considered, the V_3^{ion} potential is well separated from its neighbors at FC_{probe} and therefore V_3^{ion} was used in the simulation without any correction. Since the transition dipole moments (TDMs) computed between electronic states of different spatial symmetries are a factor of 20 lower than the TDM between V_0^{ion} and V_3^{ion} (see data in Fig. 4.22), only the electronic states V_0^{neu}, $\tilde{V}_0^{\mathrm{ion}}$, and

---

[3] The V_0^{ion} computed by the TDDFT was modified as $\tilde{V}_0^{\mathrm{ion}} = V_0^{\mathrm{ion}} + A(u)(u - u_0^{ion})^2$, where $A(u) = 80.0$ eV/Å^2 for $u > u_0^{ion}$ and $A(u) = 0.0$ otherwise.

$\mathrm{V}_3^{\mathrm{ion}}$ were considered in the simulations.

The 1D ground state vibrational eigenfunctions were determined according to the Fourier-grid Hamiltonian method [96] and the propagation was performed using the split-operator method [97, 98] together with the fast-Fourier technique [99]. The interaction with the electric field (during wave packet evolution on $\tilde{\mathrm{V}}_0^{\mathrm{ion}}$ and $\mathrm{V}_3^{\mathrm{ion}}$) was treated in the dipole approximation using the computed TDM between $\mathrm{V}_0^{\mathrm{ion}}$ and $\mathrm{V}_3^{\mathrm{ion}}$, which turned out to be constant in the region near $\mathrm{FC}_{\mathrm{probe}}$. The tunnel ionization process was simulated by a single-photon resonant transition between $\mathrm{V}_0^{\mathrm{neu}}$ and $\tilde{\mathrm{V}}_0^{\mathrm{ion}}$. Both the pump and probe pulses had $\sin^2(\mathrm{t})$ temporal intensity profiles with a full-width at half maximum (FWHM) of 20 and 40 fs, respectively. The short pump pulse was chosen to mimic tunnel ionization near the peak of the pulse.

Appendix B

Wave Packet Code

What follows is the Matlab code for generating a movie showing 2D wave packet oscillating in the potential for CH_2I_2. Potentials were calculated by Dr. Tamás Rozgonyi. The two-dimensional $CH_2I_2^+$ potential used for calculating the wave packet as a function of time is shown in Fig. 4.23. However, this code can be adapted to any two-dimensional potential, with adjustment of the time step (steeper potentials require shorter time steps for self-consistent results). The one-dimensional version is an obvious simplification of this code. Some lines have been wrapped relative to the original code, for spacing reasons. Dr. Rozgonyi independently performed similar wave packet propagations with identical results.

```
%wavepacket2D_CH2I2.m  Sarah 09/01/07
%written to allow the evolution of a wave packet in a
%2D potential well of arbitrary shape
%All numbers are in atomic units!!!
%This implementation is specifically for
%CH2I2 calculations using Dr. Rozgonyi's PESs.

%clear any previous variables from memory
clear all

% load the x-variable
% loaded axis is in Angstroms, so must be converted
length_const=0.529; %a_0=5.29e-11 m
x_ang=load('big_R_axis_256'); %Symmetric Stretch
%x_ang=load('x_b_asym_128');  %Asymmetric Stretch
x=x_ang./length_const;
xstepsize=x(2)-x(1);
```

```
xrange=max(x)-min(x) + xstepsize;

% load the y-variable
% loaded axis is in Angstroms, so must be converted
y_ang=load('little_r_axis_256'); %Symmetric Stretch
%y_ang=load('y_a_asym_128');   %Asymmetric Stretch
y=y_ang./length_const;   %a_0=5.29e-11 m
ystepsize=y(2)-y(1);
yrange=max(y)-min(y) + ystepsize;

%make the meshgrid
[X,Y]=meshgrid(x,y);

% load the potential well
% Tamas' potential
% generated by interpolating the calculation data
potential=load('fine_cationPES');  %symmetric
% potential=load('cation_asym_128x128');  %asymmetric

% plot the potential - optional
% figure
% surf(x,y,potential);shading interp;view(0,90);colorbar


%generate a normalized initial wavefunction
% uppercase Mu,R are for C_I distance (x);
% lowercase are for I_2 distance (y)
hbar=1;
%mass(I)=126.9; mass(CH_2)=14;
%mass(proton)/mass(electron)=1836.15;
% Symmetric Stretch Reduced Masses
Mu_x=(2*126.9*14/(14+2*126.9))*1836.15;
mu_y=(126.9*126.9/(2*126.9))*1836.15;

% Asymmetric Stretch Reduced Masses  (calculated by Tamas)
% Mu_x=79.32965*1836.15;
% mu_y=15.226313*1836.15;

% load the initial wave function (calculated by Tamas)
% based on the ground neutral state
```

```
psi0=load('interp_gs_wfn'); % symmetric
% psi0=load('wfn_asym_128x128_shift');  % asymmetric

%make the p-variables and fftshift them
%need a factor of 2*pi
p_x=-1/(2*xstepsize):1/xrange:1/(2*xstepsize)-1/xrange;
p_x=2*pi*fftshift(p_x);
p_y=-1/(2*ystepsize):1/yrange:1/(2*ystepsize)-1/yrange;
p_y=2*pi*fftshift(p_y);
[P_X,P_Y]=meshgrid(p_x,p_y);
P_prop=(P_X.^2/Mu_x + P_Y.^2/mu_y)/(2*hbar);

%plot the initial wavefunction - optional
% figure(100)
% hold off
% surf(x,y,psi0);shading interp; view(0,90);

% initialize data
psimat=abs(psi0);
plottime=0;
psistart=psi0;
%initialize normalized expectation values
norm=sum(sum(conj(psi0).*psi0)*xstepsize*ystepsize);
normstart=norm;
x_expt=sum(sum(conj(psi0).*psi0.*X*xstepsize*ystepsize))/norm;
y_expt=sum(sum(conj(psi0).*psi0.*Y*xstepsize*ystepsize))/norm;
wfn_overlap=sum(sum(conj(psi0).*psistart*xstepsize*ystepsize))
        /normstart;

%clear unneeded variables
clear P_X P_Y

%Do the time evolution - time steps must be "short"
time_const=2.42e-2; %fs/atomic time unit
timestep=25;
maxtime=5000;
time=0:timestep:maxtime;
% make the propagator exponentials;
% V_exp is halved for smaller error in the symmetrized product
V_exp=exp((-i*potential.*timestep)/(2*hbar));
```

```
P_exp=exp(-i*P_prop.*timestep);

%time the total propagation
tic
for n=0+timestep:timestep:maxtime
    %work with symmetrized product to make errors
    %order timestep^3 rather than timestep^2
    %do the x steps first
    psi1=V_exp.*psi0;
    psi2=fft2(psi1);
    psi3=P_exp.*psi2;
    psi4=ifft2(psi3);
    psi5=V_exp.*psi4;

    %plot the wave packet every mth iteration
    m=300;
    if rem(n,m)==0
        %make a supermatrix for plotting
        plottime=vertcat(plottime,n);
        psimat=cat(3,psimat,abs(psi5));
        %calculate normalized expectation values
        norm=sum(sum(conj(psi5).*psi5*xstepsize*ystepsize));
        new_x_expt=sum(sum(conj(psi5).*psi5.*X*xstepsize...
            *ystepsize));
        x_expt=vertcat(x_expt,new_x_expt/norm);
        new_y_expt=sum(sum(conj(psi5).*psi5.*Y*xstepsize...
            *ystepsize));
        y_expt=vertcat(y_expt,new_y_expt/norm);
        new_wfn_overlap=sum(sum(conj(psi5).*psistart...
            *xstepsize*ystepsize));
        wfn_overlap=vertcat(wfn_overlap,new_wfn_overlap...
            /normstart);
    end
    psi0=psi5;
end
toc

%plot the expectation values in fs and angstroms
fstime=plottime*time_const;
plot_x_expt=x_expt*length_const;
```

```
plot_y_expt=y_expt*length_const;
figure
plot(fstime,plot_y_expt,'b.-') %a_0=5.29e-11 m
hold on
plot(fstime,plot_x_expt,'r.-') %a_0=5.29e-11 m
xlabel('Time [fs]')
ylabel('Expectation value [Angstroms]')
legend('<r>','<R>','Location','East')

figure
plot_wfn_overlap=abs(wfn_overlap);
plot(fstime,plot_wfn_overlap,'g')
xlabel('Time [fs]')
ylabel('Wavefunction Overlap [normalized]')

% save the data
save('fstime','fstime','-ascii','-tabs');
save('x_expt','plot_x_expt','-ascii','-tabs');
save('y_expt','plot_y_expt','-ascii','-tabs');
save('wfn_overlap','plot_wfn_overlap','-ascii','-tabs');
save('supermat','psimat');

output='The supermatrix has been saved as supermat.mat in the
    current folder.'
plotboolean=input('Do you want to make a pseudomovie of the
    wavepacket? (y for yes, n for no) ','s');
if strcmp(plotboolean,'y')
    figure(103)
    hold off
    plotx=x*length_const;
    ploty=y*length_const;
    for k=1:1:size(fstime)
        plotthis=psimat(:,:,k);
        surf(plotx,ploty,abs(plotthis));
        shading interp;
        view(0,90);
        %need to fix caxis for consistency between frames
        caxis([0 4.5])
        title(strcat('Time [fs]: ',num2str(floor(fstime(k)))))
        xlabel('R [Angstroms]')
```

```
        ylabel('r [Angstroms]')
        pause(0.02);
        wavemovie(k)=getframe(gcf);
    end
    figure
    axes('Position',[0 0 1 1])
    movie2avi(wavemovie,'wavemovie.avi')
elseif strcmp(plotboolean,'n')
    output='Thank you for running wavepacket2D.m'
else
    output='You have entered an invalid response.
        The program will abort.'
    break;
end
```